

Response to Reviewer's comments on "Microphysics-based black carbon aging in a global CTM: constraints from HIPPO observations and implications for global black carbon budget" by He et al.

Referee #1

Minor Comments:

1. *"In my question 1.11 (what's the additional computational burden) I actually wanted to know an estimate how much longer it takes to run the model with the more sophisticated aging treatment."*

Response: We thank the reviewer for clarifying this comment. We would like to point out that the microphysics-based aging scheme requires a fully coupled gas-aerosol chemistry model run, while the fixed aging scheme only requires an uncoupled offline BC simulation. Thus, compared with the offline BC simulation using a fixed aging time, the coupled gas-aerosol chemistry simulation using the microphysics-based BC aging scheme increases the simulation time by a factor of five. If we run the coupled gas-aerosol chemistry simulation for both schemes, the microphysics-based BC aging scheme only takes 5-10% more simulation time than the fixed aging scheme. Thus, the major additional computational burden for the microphysics-based aging scheme comes from the requirement to run a fully coupled gas-aerosol chemistry simulation.

2. *"Somehow something went wrong with copy-and-pasting my comment 2, when I originally submitted the review, so the authors obviously could not address it. Sorry about this. I meant to write:*

"2. Setup of sensitivity studies: A potentially important sensitivity run that is missing is one that investigates the sensitivity to the assumption that 80% of the freshly emitted BC is hydrophobic (Page 32785, line 18). Can you please comment in this?" It would be great to have this clarified also."

Response: Points are well taken. We agree that assuming 80% of freshly emitted BC to be hydrophobic, which is based on previous modeling studies (Cooke et al., 1999; Park et al., 2003), could involve uncertainty. Recent observations (e.g., Willis et al., 2015) suggested that the hydrophobic BC fraction at emissions depends on the amount and type of organics coated with BC. However, considering the fast microphysical BC aging near source regions shown in this study, freshly emitted hydrophobic BC will be quickly converted to hydrophilic BC (mostly within a few hours; see Fig. 3). Thus, model results using the microphysical aging scheme may not be sensitive to the assumed hydrophobic fraction of freshly emitted BC. A more quantitative analysis on this aspect will be investigated in our future study. We have included additional discussions in Page 9, Lines

194-199 as follows:

“We assume that 80% of freshly emitted BC particles are hydrophobic (Cooke et al., 1999; Park et al., 2003). Recent observations (e.g., Johnson et al., 2005; Willis et al., 2015) showed that BC particles can be often coated with organics at emissions, suggesting that the hydrophobic fraction of freshly emitted BC particles depends on the amount and type of coated organics. Thus, the assumed fresh hydrophobic BC fraction in this study could involve uncertainty, which requires further investigation.”

3. *“In section 2.2.1.1 you introduce seven types of aerosol where secondary aerosol can condense on. In section 2.2 it says that there are also four size bins of mineral dust. Do you assume that there is no material condensing on dust?”*

Response: Yes, we assume that there is no material condensing on dust in this study, which may introduce some uncertainty. We have made clarifications on this in Page 11, Lines 237-238 as follows:

“We do not include the condensation of soluble materials on dust particles, which may introduce some uncertainty.”

1 **Microphysics-based Black Carbon Aging in a global CTM: Constraints from**
2 **HIPPO Observations and Implications for Global Black Carbon Budget**

3

4 Cenlin He¹, Qinbin Li¹, Kuo-Nan Liou¹, Ling Qi¹, Shu Tao², Joshua P. Schwarz³

5

6 ¹Department of Atmospheric and Oceanic Sciences and Joint Institute for Regional Earth
7 System Science and Engineering, University of California, Los Angeles (UCLA), Los
8 Angeles, CA 90095, USA

9 ²Laboratory for Earth Surface Processes, College of Urban and Environmental Sciences,
10 Peking University, Beijing 100871, China

11 ³Chemical Sciences Division, Earth System Research Laboratory, NOAA, Boulder, CO
12 80305, USA

13

14

15 Correspondence to: Cenlin He (cenlinhe@atmos.ucla.edu)

16

17

18 **Abstract**

19 We develop and examine a microphysics-based black carbon (BC) aerosol aging scheme
20 that accounts for condensation, coagulation, and heterogeneous chemical oxidation
21 processes in a global 3-D chemical transport model (GEOS-Chem) by interpreting the BC
22 measurements from the HIAPER Pole-to-Pole Observations (HIPPO, 2009–2011) using
23 the model. We convert aerosol mass in the model to number concentration by assuming
24 lognormal aerosol size distributions and compute the microphysical BC aging rate
25 (excluding chemical oxidation aging) explicitly from the condensation of soluble
26 materials onto hydrophobic BC and the coagulation between hydrophobic BC and
27 preexisting soluble particles. The chemical oxidation aging is tested in the sensitivity
28 simulation. The microphysical aging rate is ~4 times higher in the lower troposphere over
29 source regions than that from a fixed aging scheme with an e-folding time of 1.2 days.
30 The higher aging rate reflects the large emissions of sulfate-nitrate and secondary organic
31 aerosol precursors hence faster BC aging through condensation and coagulation. In
32 contrast, the microphysical aging is more than fivefold slower than the fixed aging in
33 remote regions, where condensation and coagulation are weak. Globally BC
34 microphysical aging is dominated by condensation, while coagulation contribution is
35 largest over East China, India, and Central Africa. The fixed aging scheme results in an
36 overestimate of HIPPO BC throughout the troposphere by a factor of 6 on average. The
37 microphysical scheme reduces this discrepancy by a factor of ~3, particularly in the
38 middle and upper troposphere. It also leads to a threefold reduction in model bias in the
39 latitudinal BC column burden averaged along the HIPPO flight tracks, with largest
40 improvements in the tropics. The resulting global annual mean BC lifetime is 4.2 days
41 and BC burden is 0.25 mg m^{-2} , with 7.3% of the burden at high altitudes (above 5 km).
42 Wet scavenging accounts for 80.3% of global BC deposition. We find that in source
43 regions the microphysical aging rate is insensitive to aerosol size distribution,
44 condensation threshold, and chemical oxidation aging, while it is the opposite in remote

45 regions, where the aging rate is orders of magnitude smaller. As a result, global BC
46 burden and lifetime show little sensitivity (<5% change) to these three factors.
47

48 **1. Introduction**

49 Black carbon (BC) aerosol is one of the most important contributors to current global and
50 regional warming (Bond et al., 2013). BC directly absorbs solar radiation, leading to
51 significant atmospheric warming (Ramanathan and Carmichael, 2008). It also acts as
52 cloud condensation nuclei (CCN), affecting cloud formation and distribution (Jacobson,
53 2014). Additionally, BC reduces snow albedo after deposition on snow, resulting in
54 accelerated snow melting (Painter et al., 2013; Liou et al., 2014). The assessment by
55 Bond et al. (2013) pointed out that current estimates of BC climatic effects involve large
56 uncertainties. One of the critical uncertainty sources is BC atmospheric aging through the
57 physical and chemical transformation of BC from hydrophobic to hydrophilic particles.

58

59 BC is emitted mostly as hydrophobic particles externally mixed with other aerosol
60 constituents (Zhang et al., 2008). Recent studies showed that BC can also be frequently
61 mixed with organics even at emission under specific conditions (Willis et al., 2015 and
62 references therein). Hydrophobic BC becomes hydrophilic due to increasing internal
63 mixing with water-soluble materials through condensation (Moteki et al., 2007),
64 coagulation (Johnson et al., 2005), and heterogeneous oxidation (Khalizov et al., 2010)
65 during atmospheric aging. Hereinafter we refer to these internal mixtures generically as
66 “coatings” without making any specific reference to mixing morphology. Coating
67 enhances BC absorption and scattering capacities (Bond et al., 2006), which depends on
68 coating properties and particle morphology (Scarnato et al., 2013; He et al., 2015).
69 Coated BC particles typically have a higher hygroscopicity (Zhang et al., 2008) and
70 hence more efficient wet scavenging, which further affects BC atmospheric lifetime
71 (Zhang et al., 2015). Thus, BC aging is expected to play a critical role in affecting both
72 BC optical properties and global distribution.

73

74 In global chemical transport models (CTMs), BC aging is typically parameterized by a

75 fixed e-folding time of 1–2 days for the hydrophobic-to-hydrophilic BC conversion (e.g.,
76 Chung and Seinfeld, 2002; Koch et al., 2009; Q. Q. Wang et al., 2011, 2014). However,
77 Koch et al. (2009) and Schwarz et al. (2013) showed that most global models
78 significantly deviate from observed global BC distributions. It is likely that the
79 prescription of uniform BC aging timescales may be partially contributing to such biases.
80 In this vein, Shen et al. (2014) optimized the fixed e-folding aging time of BC by fitting a
81 global CTM results to HIPPO observations. They suggested that anthropogenic BC from
82 East Asia ages much faster than one day, while the aging of biomass burning BC from
83 Southeast Asia is much slower. Using another global CTM constrained by HIPPO
84 observations, Zhang et al. (2015) pointed out that the optimized e-folding aging time
85 following Shen et al. (2014) varies significantly for BC emitted from different source
86 regions, with less than half a day for BC emitted from the tropics and mid-latitudes and
87 ~1 week for BC emitted from high latitudes. Thus, a uniform BC aging time is likely not
88 representative and can conceivably lead to large uncertainties.

89

90 In addition, field measurements have shown that a fixed e-folding time of 1–2 days
91 underestimates the BC aging rate in polluted areas and is unrepresentative under complex
92 atmospheric conditions. For example, Johnson et al. (2005) found that ambient BC
93 particles that underwent aging for less than a few hours were heavily coated in Mexico
94 City, primarily with ammonium sulfate. Schwarz et al. (2008) showed that 60–80% of BC
95 particles are coated in fresh emissions from biomass burning sources. Moffet and Prather
96 (2009) observed a BC aging time of ~3 hours in Mexico City under photochemically
97 active conditions. Akagi et al. (2012) showed that the fraction of coated BC particles
98 produced from a chaparral fire in California increased up to ~85% over a 4-hour period.
99 Therefore, it is imperative to better capture BC aging rate under different atmospheric
100 conditions in order to accurately estimate BC spatiotemporal distribution and
101 consequently its radiative effects.

102

103 To that end, several global models have treated BC aging with size-resolved aerosol
104 microphysics (e.g., Jacobson, 2010; Aquila et al., 2011). Many global models still rely on
105 relatively simple parameterizations for BC aging (e.g., Riemer et al., 2004; Liu et al.,
106 2011; Oshima and Koike, 2013) in part for computational efficiency consideration. For
107 example, Riemer et al. (2004) developed a BC aging parameterization in which aging rate
108 was a function of total number concentration of secondary inorganic particles and
109 internally mixed BC particles, representing the effects of condensation and coagulation
110 processes. Liu et al. (2011) proposed another parameterization in which BC aging rate
111 was a linear function of hydroxyl radical (OH) concentration (i.e., a fast-aging term
112 representing condensation of sulfuric acid) with a constant slow-aging term (e.g.,
113 coagulation). Croft et al. (2005) and Huang et al. (2013) further employed these two
114 parameterizations in a global model to estimate aging effects on BC budget and lifetime.
115 However, there are limitations in these simplified aging parameterizations. The Riemer et
116 al. (2004) parameterization was designed specifically for domains dominated by fossil
117 fuel emissions, which may not be suitable for application to a global scale. The Liu et al.
118 (2011) formulation neglected the dependencies of BC aging on different condensable
119 materials and their precursors (e.g., SO₂). Furthermore, under complex atmospheric
120 conditions, these parameterizations likely introduce large uncertainties by lumping
121 microphysical details of BC aging into a few parameters. Incorporating explicit
122 microphysical representations of the BC aging process in global models may partially
123 rectify and reduce the uncertainties.

124

125 In this study, we develop a “hybrid” microphysics-based BC aging scheme that accounts
126 for condensation and coagulation processes in the GEOS-Chem global 3-D CTM.
127 GEOS-Chem has been widely used to simulate BC in source regions (Li et al., 2015),
128 continental outflows (Park et al., 2005), remote mountainous regions (He et al., 2014a),

129 the Arctic (Wang et al., 2011), and remote oceans (Q. Q. Wang et al., 2014). Presently
130 GEOS-Chem employs a fixed e-folding time of 1.2 days for the BC aging (Park et al.,
131 2003). We convert aerosol mass in the model to number concentration by assuming
132 lognormal aerosol size distributions and explicitly compute the microphysical BC aging
133 rate from the condensation of soluble materials onto hydrophobic BC and the coagulation
134 between hydrophobic BC and preexisting hydrophilic particles. The ‘hybrid’
135 microphysical aging scheme thus not only takes account of the microphysical aging
136 processes but also avoids the use of full-fledged dynamic aerosol microphysics thereby
137 retains the computational efficiency of the fixed e-folding time aging scheme. The
138 ‘hybrid’ microphysical aging scheme can be similarly applied in other CTMs. We
139 systematically examine BC simulations using the aging scheme by comparison with the
140 HIAPER Pole-to-Pole Observations (HIPPO) of BC during 2009–2011. We further
141 analyze the effects of the aging scheme on global BC lifetime and budget. Finally, we
142 quantify the uncertainties associated with key parameters in the aging scheme and the
143 effects of chemical oxidation on BC aging.

144

145 **2. Methods**

146 **2.1 Observations**

147 We use the HIPPO aircraft measurements (Wofsy et al., 2011) of BC in this study. HIPPO
148 (<http://hippo.ornl.gov/>) provides unique constraints on BC distributions from the surface
149 up to ~14 km across the Pacific from 67°S to 85°N latitudes. There were five
150 deployments during 2009–2011 (Fig.1, HIPPO 1: January 8–30, 2009; HIPPO 2: October
151 30 – November 22, 2009; HIPPO 3: March 24 – April 16, 2010; HIPPO 4: June 14 – July
152 11, 2011; HIPPO 5: August 9 – September 9, 2011). The refractory BC (rBC) mass
153 concentration was measured by a single-particle soot photometer (SP2) that detects
154 individual particles (Schwarz et al., 2010, 2013). SP2 measures rBC in a mass range
155 corresponding to volume-equivalent diameter range of ~90–550 nm assuming 1.8 g/cc

156 void free density. This range contains about 90% of the total BC mass in the
157 accumulation mode. The observed rBC concentration was scaled upwards by 10% to
158 account for BC particles undetected by SP2 (Schwarz et al., 2010) in this mode. rBC is
159 experimentally equivalent to elemental carbon at the 15 % level (Kondo et al., 2011), and
160 hence is equivalent to BC in the model. The effective detection limit (2σ level) is 0.01 ng
161 kg^{-1} (0.1 ng kg^{-1}) for 15-minute (1-minute) sampling at low altitudes and increase to 0.05
162 (0.5 ng kg^{-1}) at the higher altitudes (Schwarz et al., 2013). The SP2 measurement of rBC
163 mass is insensitive to non-BC mass and not influenced by other absorbing particles such
164 as dust or non-absorbing species including salt and sulfate. Schwarz et al. (2013)
165 determined a total systematic uncertainty of 30% associated with rBC mass concentration
166 measured with the SP2. Schwarz et al. (2010, 2013) provided details of the BC
167 measurement during HIPPO. We average the BC observations that are located within
168 each model grid and over the model transport time step (15 minutes), thus ensuring a
169 consistent spatiotemporal resolution for direct comparison with the model results.

170

171 **2.2 Model description and simulations**

172 In this study, we use the GEOS-Chem model (version 9-01-03) driven by assimilated
173 meteorological fields from the Goddard Earth Observing System (GEOS-5) of the NASA
174 Global Modeling and Assimilating Office (GMAO). GEOS-5 meteorological fields have
175 a 6-hour temporal resolution (3 hours for surface variables and mixing depths), a native
176 horizontal resolution of $0.5^\circ \times 0.667^\circ$, and 72 vertical layers (from the surface to 0.01 hPa).
177 The spatial resolution is degraded to $2^\circ \times 2.5^\circ$ horizontally and 47 layers vertically for
178 computational efficiency. GEOS-Chem includes a fully coupled treatment of tropospheric
179 O_3 - NO_x -VOC chemistry, sulfate-nitrate-ammonia and carbonaceous aerosols. Park et al.
180 (2003) presented the first GEOS-Chem simulation of carbonaceous aerosols including
181 BC and organic carbon (OC). The model also accounts for other aerosols including
182 secondary organic aerosol (SOA), dust, and sea salt. GEOS-Chem uses a bulk aerosol

183 scheme that separately tracks mass concentrations of different aerosol species (i.e.,
 184 externally mixed). The model resolves hydrophobic and hydrophilic BC and OC,
 185 fine-mode (0.01–0.5 μm) and coarse-mode (0.5–8.0 μm) sea salt, dust in four size bins
 186 (0.1–1.0, 1.0–1.8, 1.8–3.0, and 3.0–6.0 μm), and five types of lumped SOA formed from
 187 different precursors. Aerosol and gas phase simulations are coupled through formation of
 188 sulfate, nitrate, and SOA, heterogeneous chemistry, and aerosol effects on photolysis
 189 rates. Details on the GEOS-Chem aerosol simulations are provided, respectively, by Park
 190 et al. (2003) for BC and OC, Park et al. (2004) for sulfate-nitrate-ammonia, Liao et al.
 191 (2007) for SOA, Fairlie et al. (2007) for dust, and Alexander et al. (2005) for sea salt.

192

193 **2.2.1 A microphysics-based BC aging scheme**

194 We assume that 80% of freshly emitted BC particles are hydrophobic (Cooke et al., 1999;
 195 Park et al., 2003). Recent observations (e.g., Johnson et al., 2005; Willis et al., 2015)
 196 showed that BC particles can be often coated with organics at emissions, suggesting that
 197 the hydrophobic fraction of freshly emitted BC particles depends on the amount and type
 198 of coated organics. Thus, the assumed fresh hydrophobic BC fraction in this study could
 199 involve uncertainty, which requires further investigation. Presently BC aging process is
 200 not explicitly represented in GEOS-Chem. Instead, a fixed e-folding time (τ) of 1.2 days
 201 is assumed for the hydrophobic-to-hydrophilic BC conversion in the forms (Park et al.,
 202 2003):

$$203 \quad \left(\frac{dm_{BCPO}}{dt} \right) = - \frac{m_{BCPO}}{\tau} \quad (1)$$

$$204 \quad \left(\frac{dm_{BCPI}}{dt} \right) = - \left(\frac{dm_{BCPO}}{dt} \right) \quad (2)$$

205 where m_{BCPO} and m_{BCPI} are the mass concentration of hydrophobic (BCPO) and
 206 hydrophilic BC (BCPI), respectively. In this study, we develop a microphysics-based BC
 207 aging scheme in the model by explicitly accounting for both condensation and

208 coagulation processes. This microphysical aging scheme can be similarly applied in other
 209 CTMs. Additionally, we incorporate an experiment-based parameterization for BC aging
 210 through heterogeneous chemical oxidation (Pöschl et al., 2001) for comparison and
 211 contrast.

212

213 2.2.1.1 Condensation

214 The condensation rate of a gaseous species (A) onto an individual particle can be
 215 expressed as follows (Seinfeld and Pandis, 2006):

$$216 \quad J_{A,p} = 4\pi f(K_n, \alpha) R_p D_{f_A} (c_\infty - c_s) \quad (3)$$

$$217 \quad f(K_n, \alpha) = \frac{1 + K_n}{1 + 2K_n(1 + K_n)/\alpha} \quad (4)$$

218 where $J_{A,p}$ is the condensation rate (mol s^{-1}) of A onto a particle, R_p represents the particle
 219 radius (m), D_{f_A} is the gas-phase diffusivity ($\text{m}^2 \text{s}^{-1}$) of A , c_∞ and c_s are gas-phase
 220 concentrations (mol m^{-3}) of A far from the particle and at the particle surface, respectively.
 221 K_n is the Knudsen number (i.e., ratio of air mean free path to particle radius), α is the
 222 accommodation coefficient ($\alpha = 1$ in this study), and $f(K_n, \alpha)$ is the correction factor for
 223 non-continuum effects and imperfect surface accommodation based on the mathematical
 224 expression from Dahneke (1983). The mass of A condensing onto BCPO in a model grid
 225 per unit time, k_A , can be calculated by the product of the total available mass of A for
 226 condensing onto all pre-existing aerosols and the fraction of condensed mass partitioned
 227 to BCPO, which depends on condensation rate (J) and particle number concentration (N)
 228 as follows:

$$229 \quad k_A = \frac{J_{A,BCPO,tot}}{\sum_{p_i=1}^{p_i=7} J_{A,p_i,tot}} M_{A,cond} = \frac{\int_0^\infty n_{BCPO}(R_{BCPO}) f_{BCPO}(K_n, \alpha) R_{BCPO} dR_{BCPO}}{\sum_{p_i=1}^{p_i=7} \int_0^\infty n_{p_i}(R_{p_i}) f_{p_i}(K_n, \alpha) R_{p_i} dR_{p_i}} M_{A,cond} \quad (5)$$

230 where p_i ($i = 1-7$) represents seven types of pre-existing aerosols (i.e., BCPO, BCPI,
 231 hydrophobic OC, hydrophilic OC, sulfate, fine-mode and coarse-mode sea salt) available

232 for condensation, $J_{A,p_i,tot}$ is the condensation rate of A onto particle p_i , $M_{A,cond}$ is the
 233 total condensed mass of A in a model grid per unit time, R_{p_i} and n_{p_i} ($= dN_{p_i}/dR_{p_i}$) are
 234 the radius and number concentration distribution function of pre-existing particles,
 235 respectively. We account for condensation of gaseous sulfuric acid (H_2SO_4), nitric acid
 236 (HNO_3), ammonia (NH_3), and SOA onto pre-existing BC, OC, sulfate (SO_4^{2-} , NO_3^- , and
 237 NH_4^+), and sea salt aerosols. We do not include the condensation of soluble materials on
 238 dust particles, which may introduce some uncertainty.

239

240 GEOS-Chem tracks only aerosol mass concentration rather than number concentration
 241 that is required in Eq. (4). We convert aerosol mass concentration (m_{p_i}) to number
 242 concentration (N_{p_i}), assuming lognormal distributions for different aerosols following
 243 Croft et al. (2005) in the form:

$$244 \quad N_{p_i} = \frac{m_{p_i}}{\rho_{p_i}} \left(\frac{\pi}{6} D_{p_i}^3 \exp\left(\frac{9}{2} \ln^2 \sigma_{p_i}\right) \right)^{-1} \quad (6)$$

245 where ρ_{p_i} is the particle density (1.8 g cm⁻³ for BC and OC, 1.7 g cm⁻³ for sulfate, and
 246 2.2 g cm⁻³ for sea salt), D_{p_i} and σ_{p_i} are the geometric mean diameter and standard
 247 deviation of number size distribution, respectively. Following Dentener et al. (2006) and
 248 Yu and Luo (2009), we assume $D_p = 60$ nm and $\sigma_p = 1.8$ for BCPO and hydrophobic OC,
 249 and $D_p = 150$ nm and $\sigma_p = 1.8$ for BCPI and hydrophilic OC (Table 1). We use size
 250 distributions from the Global Aerosol Dataset (GADS) (Koepke et al., 1997) for sulfate
 251 ($D_p = 150$ nm, $\sigma_p = 1.6$), fine sea salt ($D_p = 200$ nm, $\sigma_p = 1.5$), and coarse sea salt ($D_p =$
 252 800 nm, $\sigma_p = 1.8$). In order to analytically compute the integral in Eq. (5), we have
 253 assumed a constant correction factor $f(K_n, \alpha)$ for each type of aerosols with different sizes,
 254 which may introduce uncertainty in the computation. Under this assumption and using a
 255 lognormal aerosol size distribution, the integral can now be computed by following the

256 mathematical identity:

$$257 \int_0^\infty n_{p_i}(R_{p_i})R_{p_i}dR_{p_i} = N_{p_i} \frac{D_{p_i}}{2} \exp\left(\frac{1}{2} \ln^2 \sigma_{p_i}\right) \quad (7)$$

258 The hydrophobic-to-hydrophilic BC conversion rate ($\text{kg m}^{-3} \text{ s}^{-1}$) due to condensation can
259 be written as

$$260 \left(\frac{dm_{BCPO}}{dt}\right)_{cond} = -\frac{F_{BCPO \rightarrow BCPI} m_{BCPO}}{\Delta t} \quad (8)$$

$$261 F_{BCPO \rightarrow BCPI} = \frac{\sum_{A_i=1}^{A_i=4} k_{A_i} \cdot \Delta t}{\beta M_{BCPO}} \quad (9)$$

262 where $F_{BCPO \rightarrow BCPI}$ represents the fraction of BCPO becoming BCPI through condensation
263 of four types of soluble species A_i ($i = 1-4$, i.e., H_2SO_4 , HNO_3 , NH_3 , and SOA) in a
264 model time step (Δt). This implicitly assumes that different secondary aerosol species
265 have the same hygroscopicity. We note that some SOA species could be less hygroscopic
266 than ammonia sulfate (Prenni et al., 2007). m_{BCPO} is BCPO mass concentration (kg m^{-3}),
267 M_{BCPO} is the total BCPO mass (kg) in a model grid, and β is the condensation threshold
268 (i.e., the mass fraction of condensed soluble materials on BCPO required for the
269 hydrophobic-to-hydrophilic conversion). Following Riemer et al. (2004), we set $\beta = 5\%$
270 in the standard simulation based on hygroscopic growth behavior of aerosols
271 (Weingartner et al., 1997). After the hydrophobic-to-hydrophilic BC conversion, we lump
272 the mass of secondary aerosol material coated on BC with those not mixed with BC in
273 order to be compatible with the bulk aerosol scheme in GEOS-Chem, where the mass
274 concentration of different aerosol species are separately tracked. The lumping, instead of
275 treating coating materials and hydrophilic BC together, only introduces small uncertainty,
276 considering that the size distribution of hydrophilic BC is similar to that of SOA and
277 sulfate in this study (see Table 1). Further sensitivity analysis also show minor effects of
278 the hydrophilic aerosol size distribution on global BC concentration and lifetime (see
279 Sect. 4.3). The use of global uniform particle size distributions and β value can

280 conceivably introduce large uncertainties. To quantify the uncertainties, we conduct
 281 additional model simulations by varying the size distribution and β value (see Table 1 and
 282 Sect. 4).

283

284 2.2.1.2 Coagulation

285 The coagulation rate ($J_{BCPO,X}$, $\text{m}^{-3} \text{s}^{-1}$) between BCPO and hydrophilic particles (X) can be
 286 expressed by (Seinfeld and Pandis, 2006)

$$287 \quad J_{BCPO,X} = \gamma K_{BCPO,X} N_{BCPO} N_X \quad (10)$$

$$288 \quad K_{BCPO,X} = 4\pi(R_{BCPO} + R_X)(D_{f_{BCPO}} + D_{f_X}) \quad (11)$$

289 where N_{BCPO} and N_X are number concentrations (m^{-3}) of BCPO and particle X computed
 290 from Eq. (6), $K_{BCPO,X}$ is the coagulation coefficient ($\text{m}^3 \text{s}^{-1}$) that depends on particle radius
 291 (R_{BCPO} and R_X) and Brownian diffusivities ($D_{f_{BCPO}}$ and D_{f_X}), and γ (from 0.014 for
 292 0.001 μm particles to 1.0 for 1 μm particles) is a correction factor that accounts for
 293 kinetic effects of small particles. We use geometric mean radii for R_{BCPO} and R_X , which
 294 could introduce uncertainty for particle sizes largely deviating from the mean value. We
 295 note that the resulting uncertainty in BC concentration and lifetime is likely small,
 296 because model results show that coagulation only makes a small contribution to the total
 297 BC aging rate over the globe (see Sect. 3.1) and the global BC distribution is insensitive
 298 to aerosol size distribution in this study (see Sects. 4.2 and 4.3). The
 299 hydrophobic-to-hydrophilic BC conversion rate through coagulation can be written in the
 300 form:

$$301 \quad \left(\frac{dN_{BCPO}}{dt} \right)_{coag} = - \sum_{p_j=1}^{p_j=6} \gamma_{p_j} K_{BCPO,p_j} N_{p_j} N_{BCPO} \quad (12)$$

302 where p_j ($j = 1-6$) represents six types of hydrophilic particles, including
 303 sulfate-nitrate-ammonia, BCPI, hydrophilic OC, SOA, fine-mode and coarse-mode sea
 304 salt. We assume that BCPO is converted to BCPI upon coagulating with these hydrophilic

305 aerosols. The resulting BCPO mass change per unit time ($\text{kg m}^{-3} \text{s}^{-1}$) is given by:

$$306 \quad \left(\frac{dm_{BCPO}}{dt} \right)_{coag} = \frac{\pi}{6} \rho_{BCPO} D_{BCPO}^3 \exp\left(\frac{9}{2} \ln^2 \sigma_{BCPO}\right) \left(\frac{dN_{BCPO}}{dt} \right)_{coag} \quad (13)$$

307

308 2.2.1.3 Chemical oxidation

309 To account for the BC aging through ozone oxidation on the BC surface, we follow an
 310 experiment-based parameterization by Pöschl et al. (2001). The same parameterization
 311 has been used in previous studies (Croft et al., 2005; Huang et al., 2013). The chemical
 312 hydrophobic-to-hydrophilic BC conversion rate ($\text{kg m}^{-3} \text{s}^{-1}$) can be expressed by

$$313 \quad \left(\frac{dm_{BCPO}}{dt} \right)_{chem} = -k_{chem} m_{BCPO} \quad (14)$$

314 where k_{chem} is the reaction rate coefficient (s^{-1}) given by

$$315 \quad k_{chem} = \frac{\lambda K_{\infty} K_{O_3} [O_3]}{1 + K_{O_3} [O_3] + K_{H_2O} [H_2O]} \quad (15)$$

316 where K_{∞} ($= 0.015 \text{ s}^{-1}$) is the pseudo-first-order decay rate coefficient in the presence of
 317 high ozone concentrations, K_{O_3} ($= 2.8 \times 10^{-13} \text{ cm}^3$) and K_{H_2O} ($= 2.1 \times 10^{-17} \text{ cm}^3$) are the
 318 adsorption rate coefficients of O_3 and H_2O , which are a function of available adsorption
 319 sites residence time, and sticking coefficients of O_3 and H_2O on BC surface. λ ($= 0.01$) is
 320 the physical shielding factor that accounts for the fact that the oxidized coating material is
 321 not distributed homogenously over the BC particle surface (Croft et al., 2005). $[O_3]$ and
 322 $[H_2O]$ are atmospheric concentrations (molec cm^{-3}) of O_3 and H_2O , respectively.

323

324 Recent experimental studies also confirmed that BC can be aged through heterogeneous
 325 chemical oxidation by O_3 (Decesari et al., 2002; Zuberi et al., 2005) and NO_2 (Khalizov
 326 et al., 2010), which results in the formation of soluble organic compounds on BC particle
 327 surface. However, none of these recent studies have given explicit quantitative
 328 parameterizations for BC chemical aging, which can be applied in modeling studies.

329 Moreover, experimental results presented in these studies vary substantially, suggesting
330 that BC chemical aging process could involve large uncertainty. For this reason, the
331 parameterization scheme developed by Pöschl et al. (2001) should be used with caution.

332

333 **2.2.1.4 Total BC aging rate**

334 We assume a linear combination of the condensation, coagulation, and chemical
335 oxidation processes, following Croft et al. (2005) and Huang et al. (2013). The total BC
336 aging rate can thus be expressed in the forms:

$$337 \quad \left(\frac{dm_{BCPO}}{dt} \right)_{mic} = \left(\frac{dm_{BCPO}}{dt} \right)_{cond} + \left(\frac{dm_{BCPO}}{dt} \right)_{coag} \quad (16)$$

$$338 \quad \left(\frac{dm_{BCPO}}{dt} \right)_{mic+chem} = \left(\frac{dm_{BCPO}}{dt} \right)_{mic} + \left(\frac{dm_{BCPO}}{dt} \right)_{chem} \quad (17)$$

339 where the subscripts *mic* and *chem* represent microphysical and chemical aging,
340 respectively. Such linear combination may overestimate BC aging rate, because these
341 processes likely compete with each other rather than occur independently (Croft et al.,
342 2005). However, no observational evidence is currently available to quantify interactions
343 among these processes.

344

345 **2.2.2 BC emissions**

346 We use a global anthropogenic BC emission inventory developed by R. Wang et al. (2014)
347 (hereinafter the PKU-BC inventory), with an annual emission of 8.5 TgC for 2008 (see
348 Fig. S1). PKU-BC incorporates a recent global high-resolution (0.1°×0.1°) fuel
349 combustion dataset (Wang et al., 2013) that covers 64 types of combustion based on local
350 or national fuel statistics. The dataset significantly improves the spatial resolution of
351 emission distribution for large countries. In addition, the inventory uses updated BC
352 emission factors based on up-to-date measurements, particularly for developing countries
353 (Wang et al., 2012a, b). The use of local and subnational fuel data and updated emission

354 factors results in 70% higher global anthropogenic BC emissions than previous
355 bottom-up inventories (4.9 ± 0.4 TgC) (Dentener et al., 2006; Bond et al., 2007; Lamarque
356 et al., 2010; Granier et al., 2011) yet still 20% lower than top-down estimates (Bond et al.,
357 2013). The PKU-BC emissions are 58% higher than the global anthropogenic emissions
358 used in our previous studies (He et al., 2014a, b). R. Wang et al. (2014) found that using
359 PKU-BC reduces the bias in modeled surface BC concentrations by up to 25% in Asia,
360 Africa, and Europe. However, Bond et al. (2013) pointed out that current anthropogenic
361 BC emission estimates are associated with large uncertainties (more than a factor of 2
362 across different inventories). Based on a Monte Carlo estimation, R. Wang et al. (2014)
363 showed an uncertainty range (interquartile) of -40% to +70% for global annual
364 anthropogenic BC emissions in PKU-BC, where errors in emission factors dominate the
365 overall uncertainty.

366

367 We use the Global Fire Emissions Database version 3 (GFED3) (van der Werf et al., 2010)
368 for global biomass burning emissions (see Fig. S1), which now includes small fire
369 emissions (Randerson et al., 2012). Carbon emissions in GFED3 increase by 35%
370 globally when small fires are included. In this study, the GFED3 emissions with a 3-hour
371 temporal resolution are used. The uncertainty in GFED3 is $\geq 20\%$ globally and highest in
372 boreal regions and Equatorial Asia, primarily because of insufficient data on fuel load,
373 emission factor, and burned area (van der Werf et al., 2010; Randerson et al., 2012).

374

375 **2.2.3 BC deposition**

376 Aerosol dry deposition follows a standard resistance-in-series scheme (Wesely, 1989),
377 which depends on local surface type and meteorological conditions, as implemented by
378 Wang et al. (1998). Wang et al. (2011) further updated aerosol dry deposition velocity
379 over snow- and ice-covered regions for improved BC simulations in GEOS-Chem. They
380 applied a constant value of 0.03 cm s^{-1} , within the range ($0.01\text{--}0.07 \text{ cm s}^{-1}$) employed in

381 previous studies (Liu et al., 2011). In the GEOS-Chem simulations presented here, dry
382 deposition accounts for ~20% of global BC deposition, consistent with the results
383 (17–23%) from previous studies using GEOS-Chem (He et al., 2014a; Q. Q. Wang et al.,
384 2014) and that (21.4±17%) from the AeroCom multi-model study (Textor et al., 2006).

385

386 Liu et al. (2001) first described aerosol wet scavenging in GEOS-Chem. Wang et al.
387 (2011) updated in the model the below-cloud scavenging parameterization for fine and
388 coarse aerosol modes by distinguishing between aerosol removals by snow and by rain.
389 Different in-cloud scavenging schemes have also been applied to cold and warm clouds,
390 with an improved areal fraction of model grids that experience precipitation (Wang et al.,
391 2011). Following Q. Q. Wang et al. (2014), we further update in-cloud scavenging of
392 water-soluble aerosols by accounting for homogeneous and heterogeneous freezing
393 nucleation in cold clouds.

394

395 **2.2.4 Model simulations**

396 To investigate the effects of the microphysics-based BC aging scheme, we first conduct
397 two GEOS-Chem BC simulations with the fixed aging (e-folding time of 1.2 days)
398 scheme (FIX, Table 1; see also Eq. (1)) and the standard microphysics-based scheme
399 (MP_{STD}, Table 1; see also Eq. (16)). In addition, we conduct 11 sensitivity simulations for
400 the microphysics-based scheme to quantify the effects of chemical oxidation on BC aging
401 and the uncertainty associated with aerosol size distribution and condensation threshold
402 in the microphysics-based scheme. Specifically, we combine the standard
403 microphysics-based scheme with the Pöschl et al. (2001) parameterization for chemical
404 oxidation to examine the effects of chemical oxidation on BC aging (MP_{chem}, Table 1; see
405 also Eq. (17)). We use geometric mean diameters of 30 nm and 90 nm for BCPO number
406 size distribution as lower and upper bounds ($D_{\text{BCPO}30}$ and $D_{\text{BCPO}90}$, Table 1), following
407 Bond et al. (2006), instead of 60 nm in the standard simulation (i.e., MP_{STD}). We use

408 geometric standard deviations of 1.4 and 2.0 for BCPO number size distribution as lower
409 and upper bounds ($SD_{BCPO1.4}$ and $SD_{BCPO2.0}$, Table 1), following Bond et al. (2006),
410 instead of 1.8 in the standard simulation. We vary the geometric mean diameters and
411 standard deviations of all hydrophilic particles' number size distribution in the standard
412 simulations by $\pm 50\%$ ($D_{PI+50\%}$ and $D_{PI-50\%}$, Table 1) and ± 0.2 ($SD_{PI+0.2}$ and $SD_{PI-0.2}$,
413 Table 1). We vary the condensation threshold (β in Eq. (7)) from 5% in the standard
414 simulation to 2.5% (BETA2.5, Table 1) and to 10% (BETA10, Table 1). Model results
415 used for comparison with HIPPO observations are sampled along the HIPPO flight
416 tracks.

417

418 **3. Results and discussions**

419 **3.1 BC aging rate**

420 Figure 2 shows model simulated surface-layer and zonal distributions of annual mean
421 aging rate with the fixed (r_{fix} , calculated by Eq. 1) and microphysics-based (r_{mic} ,
422 calculated by Eq. 16) aging schemes. The maximum rates are in the surface layer over
423 major BC source regions such as Eastern China, India, Europe, eastern United States, and
424 tropical Africa, ranging from less than $100 \text{ ngC m}^{-3} \text{ h}^{-1}$ for the fixed scheme (Fig. 2a) to
425 $100\text{-}500 \text{ ngC m}^{-3} \text{ h}^{-1}$ for the microphysics-based scheme (Fig. 2b). r_{mic} is 2-6 times
426 higher than r_{fix} throughout the year over both continents and oceanic areas with heavy
427 marine traffic (Fig. S2). This is primarily because of the strong anthropogenic emissions
428 of SO_2 , NO_x , and NH_3 in major continents and along shipping corridors in the Northern
429 Hemisphere (Park et al., 2004) and biomass burning emissions of SOA precursors in
430 tropical continents (Guenther et al., 2006). These emissions lead to fast BC aging through
431 both condensation of soluble materials (i.e., $\text{H}_2\text{SO}_4\text{-HNO}_3\text{-NH}_3$ and SOA) and
432 coagulation with hydrophilic particles.

433

434 Figure 3 shows the probability density function (PDF) of simulated annual mean BC

435 e-folding aging time (τ in Eq. 1) over the globe. The first PDF peak around $\tau = 8$ h
436 represents the fast aging near source regions, while the second bump corresponds to $\tau =$
437 ~ 1 day, which reflects the aging over rural areas and in the middle troposphere. The third
438 small bump is around $\tau = 100$ h, mainly representing the very slow aging in remote
439 regions (e.g., Polar regions and the upper troposphere). The microphysics-based scheme
440 results in an e-folding BC aging time of 0.6–2 hours in summer and 1–3 hours in winter
441 when averaged within the boundary layer over major anthropogenic source regions
442 including Eastern China, eastern United States, and Europe. These are much faster than
443 the timescale of 1–2 days typically assumed in many global models (Chung and Seinfeld,
444 2002; Koch et al., 2009; He et al., 2014a). Such fast aging for anthropogenic BC has been
445 reported in previous studies. For example, Riemer et al. (2004) used a size-resolved
446 aerosol model to show an e-folding BC aging time of ~ 2 -hour during the day from 250 to
447 1500 m above source (urban) regions for both summer and winter. Jacobson (2010) also
448 reported a ~ 3 -hour e-folding aging time for fossil-fuel BC based on a global size-resolved
449 aerosol model. Shen et al. (2014) found that the e-folding aging timescale of
450 anthropogenic BC from East Asia is several hours, based on constraints from the HIPPO
451 observations. In addition, Akagi et al. (2012) observed that $\sim 20\%$ of BC ages within one
452 hour after emission in a biomass-burning plume over California in November 2009,
453 whereas our microphysics-based scheme shows a mean BC aging rate of $24\% \text{ h}^{-1}$ within
454 the same region and time period. Moteki et al. (2007) measured a BC aging rate of 2.3%
455 h^{-1} downwind of an urban area in Japan in March 2004. Though not a direct comparison,
456 our microphysics-based scheme results in a BC aging rate of $10\% \text{ h}^{-1}$ averaged over the
457 same region for March 2009.

458

459 r_{mic} decreases by several orders of magnitude with increasing altitude and from
460 continents to remote oceans and the polar regions (Fig. 2). r_{fix} is a factor of 1.5–4 lower
461 than r_{mic} below 900 hPa in the tropics and middle latitudes, but more than 5 times

462 higher in the polar regions, remote oceans, and above 800 hPa throughout the year (Figs.
463 S2–S3). The annual mean r_{mic} is 50% higher than r_{fix} in the middle to lower
464 troposphere but more than fivefold lower in the middle to upper troposphere (Table 2).
465 Because the aging rates in remote regions are vanishingly small, the difference in global
466 BC distribution between the two aging schemes is thus dominated by the difference in the
467 significantly larger aging rates over the source regions (see Sect. 3.3).

468

469 Figures 4a and 4b show that condensation dominates (>70%) BC aging globally,
470 particularly in the middle to upper troposphere (500–200 hPa) and in the southern high
471 latitudes. In contrast, the contribution from coagulation is <15% throughout much of the
472 globe, with the exception of ~30% over Eastern China, India, and central Africa, where
473 relatively abundant hydrophilic aerosols are available. This is primarily because
474 hydrophilic aerosols are substantially removed by wet scavenging during the transport to
475 remote regions, thus reducing the coagulation between hydrophobic BC and hydrophilic
476 particles. Figures 4c and 4d show that the H_2SO_4 - HNO_3 - NH_3 condensation dominates
477 (>70%) the total condensation in the northern low and middle latitudes throughout the
478 troposphere and in the southern middle latitudes below 800 hPa. This is largely explained
479 by strong anthropogenic emissions of SO_2 and NO_x in the Northern Hemisphere (Park et
480 al., 2004) and global oceanic emissions of dimethylsulfide (DMS) (Lana et al., 2011).
481 The SOA condensation, however, contributes to more than 80% of the total condensation
482 over tropical continents dominated by biomass burning emissions and the southern
483 extratropics above 700 hPa, where rather limited sulfuric acid is produced.

484

485 **3.2 Model evaluation with HIPPO observations**

486 Figure 5 shows the PDF of observed and simulated BC concentrations during the HIPPO
487 measurements. Model results from the fixed aging scheme significantly overestimate BC
488 concentrations, with a PDF peak at ~15 ng kg⁻¹ (corresponding to BC in the northern

489 extratropics) that is an order of magnitude higher than the observations. The
490 microphysics-based aging scheme substantially reduces the discrepancy between
491 modeled and observed PDFs, particularly at BC concentrations of $<1 \text{ ng kg}^{-1}$ and 10–50
492 ng kg^{-1} . The remaining model bias at extremely low BC concentrations ($<0.1 \text{ ng kg}^{-1}$),
493 corresponding to regions remote from combustion influence and highly influenced by
494 tropical convection, likely reflects the inefficient BC wet scavenging in the model (Q. Q.
495 Wang et al., 2014). Statistical analysis shows that compared with the fixed aging scheme,
496 the microphysics-based aging scheme reduces the percentages of modeled BC
497 concentrations that are more than a factor of 10 and 4 higher/lower than the observations
498 from 28% to 16% and from 53% to 37%, respectively, with a better model-observation
499 correlation as well (Fig. 6). The median BC concentration (6.6 ng kg^{-1}) from the fixed
500 aging scheme is biased high by a factor of four compared with the observations (1.6 ng
501 kg^{-1}), while the microphysics-based median concentration (3.5 ng kg^{-1}) reduces the bias
502 by a factor of two.

503

504 Figure 7 shows the median vertical profiles of BC concentration in different latitude
505 bands from HIPPO observations and model simulations. The median in the northern
506 extratropics (20° – 90° N) is $5\text{--}10 \text{ ng kg}^{-1}$ near the surface and decreases to $<1 \text{ ng kg}^{-1}$
507 above 200 hPa, while the concentration is a factor of 2–10 lower in tropical regions and
508 Southern Hemisphere throughout the troposphere. This is because of strong BC emissions
509 in the Northern Hemisphere and strong wet scavenging of BC during transport to the
510 tropics and Southern Hemisphere, particularly by tropical deep convection (Q. Q. Wang
511 et al., 2014). Model results using the fixed aging scheme generally capture the
512 spatiotemporal pattern of BC median vertical profiles in the northern extratropics, but
513 overestimate the magnitude by a factor of ~ 5 on average (Figs. 7 and S4). The largest
514 model-observation absolute discrepancies ($>20 \text{ ng kg}^{-1}$) are at 900–400 hPa during
515 non-winter seasons (Fig. S4). The microphysics-based aging scheme reduces that

516 discrepancy by 2–3 times across different altitudes in the northern extratropics,
517 particularly at 900–300 hPa (Figs. 7 and S4). This is a result of the faster BC aging from
518 the microphysics-based scheme over source regions in the Northern Hemisphere (Fig. 2),
519 which increases the amount of hydrophilic BC removed by wet scavenging during the
520 transport to the free troposphere.

521

522 In the tropics (20 °S–20 °N), the median BC concentration is generally less than 1 ng kg⁻¹,
523 with small variations across different altitudes and seasons (Figs. 7 and S4). Model
524 results using the microphysics-based aging scheme reproduce the observed BC vertical
525 distributions in different seasons with discrepancies of <0.5 ng kg⁻¹, except for a 50%
526 underestimate in the lower troposphere (Figs. 7 and S5). This could be due to the
527 overestimate in GEOS-5 precipitation fields over the tropics (Molod et al., 2012).
528 Compared with the microphysics-based aging scheme, model results from the fixed aging
529 scheme overestimate BC concentration by more than fivefold above 800 hPa in the
530 tropics, particularly in summer and fall (Fig. S5). This is primarily because of the slow
531 BC aging over tropical source regions in the fixed aging scheme (Fig. S2), resulting in
532 insufficient BC wet removal and thus excessive BC transported to the free troposphere.

533

534 In the Southern Hemisphere (20 °–70 °S), the microphysics-based aging scheme improves
535 the modeled median BC vertical profiles by a factor of 2–4 throughout all altitudes and
536 seasons (Figs. 7 and S4) with the largest improvement at 600–200 hPa (Fig. S5),
537 compared with the fixed aging scheme. However, the microphysics-based model results
538 still overestimate the BC concentration above 300 hPa by ~3 times in the Southern
539 Hemisphere, probably due to inefficient in-cloud scavenging of BC in the model for ice
540 clouds or mixed-phase clouds at such high altitudes. However, we note that the ability of
541 BC to be ice nuclei is largely uncertain. For example, Cozic et al. (2008) suggested that
542 BC particles can act as efficient ice nuclei based on observations in mixed-phase clouds,

543 whereas Friedman et al. (2011) showed that BC particles are unlikely to serve as ice
544 nuclei efficiently in cold clouds based on laboratory experiments.

545

546 Figure 8 shows the observed and model simulated latitudinal and seasonal BC column
547 burden averaged along the HIPPO flight tracks. The lowest burden is in the tropics due to
548 strong wet scavenging by deep convection. It is two orders of magnitude lower than that
549 in the extratropical Northern Hemisphere. The burden in the Southern Hemisphere is
550 minimum in spring because of the wet season in the southern low latitudes (Wang and
551 Ding, 2008), while the burden in the Northern Hemisphere is maximum during the same
552 period when the impact of Asian outflow on the Pacific peaks (Schwarz et al., 2013).
553 Model results using the fixed aging scheme capture the latitudinal and seasonal trend for
554 the observations, but significantly overestimate the magnitude with a mean positive bias
555 of 194%, particularly in the Northern Hemisphere during summer and fall, as a result of
556 the model overestimate of BC vertical profiles in the Northern Hemisphere (Fig. 7). The
557 microphysics-based aging scheme reduces the model overestimate at most latitudes
558 throughout the year, with a mean positive bias of 60% and a correlation coefficient (r) of
559 0.85 with observations. The largest improvement from the microphysics-based scheme is
560 in the tropics (Fig. 8), except in January.

561

562 Therefore, the microphysics-based aging scheme substantially improves BC simulations
563 pole-to-pole over the Pacific during HIPPO, both spatially and temporally, compared
564 with the fixed aging scheme. The remaining model-observation discrepancy, particularly
565 in the northern extratropics and the upper troposphere, is likely a result of the uncertainty
566 associated with BC emissions, wet scavenging, and model meteorological fields (Molod
567 et al., 2012; Bond et al., 2013; Q. Q. Wang et al., 2014). We note that it is important to
568 quantify the contribution of these factors to the model-observation discrepancies, which
569 will be investigated in our future study. Additionally, the spatiotemporal variability of the

570 observed BC concentration is significantly large within each altitude and latitude band
571 (Fig. 7), suggesting a strong dependence of BC vertical profile on sampling location and
572 time during the HIPPO aircraft measurements.

573

574 **3.3 Global BC distribution and budget**

575 Figures 9a and 9b show the annual mean global BC column burden from model results
576 using the fixed and microphysics-based BC aging schemes. Both schemes result in a
577 similar spatial distribution of BC burden, with highest values over source regions and
578 lowest values in the southern hemispheric oceans. However, BC burden from the
579 microphysics-based scheme is much smaller than that from the fixed scheme globally,
580 with the major difference over source regions throughout the year (Fig. S6). This is
581 because the maximum enhancement of BC aging rate from the microphysics-based
582 scheme is over source regions (Fig. 2), where there is a 20–60% increase of the
583 hydrophilic BC fraction in total BC particles relative to the fixed aging scheme (Fig. S7).
584 The faster hydrophobic-to-hydrophilic conversion leads to a stronger BC wet removal for
585 the microphysics-based aging scheme. As a result, the global annual mean BC load is
586 0.24 mg m^{-2} in the microphysics-based scheme, consistent with the result ($0.23 \pm 0.07 \text{ mg}$
587 m^{-2}) from the AeroCom multi-model study (Schulz et al., 2006). It is also comparable to
588 the value (0.25 mg m^{-2}) reported by Jacobson (2010), which accounted for size-resolved
589 aerosol microphysical processes. Bond et al. (2013) reported a much higher BC load
590 (0.55 mg m^{-2}) based on top-down estimated BC emissions that are 70% larger than the
591 emissions used in this study. The resulting global BC lifetime of 4.2 days from the
592 microphysics-based scheme is within the range (3.2–9.9 days) from previous studies
593 (Table 2).

594

595 Figures 9c and 9d show model simulated annual zonal mean BC concentration. The
596 concentration decreases substantially from the surface in the northern middle latitudes to

597 high altitudes and the polar regions, varying by three orders of magnitude. The
598 concentration from the microphysics-based aging scheme is smaller than that from the
599 fixed aging scheme at different latitudes and altitudes, with the largest difference (>400
600 ng m^{-3}) in the northern middle latitudes (Fig. S8). Although the microphysical aging rate
601 is much lower than the rate from the fixed aging scheme in the middle and upper
602 troposphere and the polar regions (Figs. 2 and S3), the faster microphysical aging over
603 source regions dominates the aging effects on global BC distribution, resulting in a
604 substantial reduction of BC concentration globally. As a result, the fraction of global BC
605 load above 5 km is 7.3% for the microphysics-based scheme, which is close to the lower
606 bound of the range (6.1–40%) from previous studies (e.g., Schulz et al., 2006; He et al.,
607 2014b; Q. Q. Wang et al., 2014). The relatively low BC load at high altitudes in the
608 microphysics-based scheme has a significant implication for global BC radiative effects.
609 Samset et al. (2013) showed that more than 40% of global BC direct radiative forcing is
610 contributed by BC particles above 5 km, whereas this estimate has large uncertainties
611 across various models. BC particles at high altitudes could also affect the formation and
612 distribution of cirrus clouds and thus BC indirect radiative effects (e.g., Liu et al., 2009).

613

614 **4. Uncertainty analysis**

615 **4.1 Heterogeneous chemical oxidation**

616 Figure 10 shows the annual mean contribution of chemical oxidation to the total BC
617 aging rate. The contribution is 10–30% below 900 hPa over most regions at 60 °S–60 °N
618 latitudes, particularly at low latitudes and over source regions, due partly to the strong
619 condensation-coagulation in these areas. Additionally, the relatively high humidity and
620 low ozone concentration also contribute to less efficient chemical oxidation aging in the
621 lower troposphere and the tropics, compared with the middle troposphere and the polar
622 regions (Fig. 10b). There is efficient chemical oxidation aging over the Arctic and
623 Antarctic in the middle troposphere, where water vapor is scarce and relatively abundant

624 ozone is available. This is consistent with the conclusion from Huang et al. (2013), which
625 used the same chemical oxidation scheme and showed the lowest chemical aging rate
626 over the tropics at lower altitudes and faster aging at higher altitudes including the polar
627 regions.

628

629 Compared with the standard microphysics-based aging scheme (MP_{STD}), incorporating
630 chemical oxidation (MP_{chem}) slightly (<5%) increases the total BC aging rate at
631 60°S–60°N latitudes in the lower troposphere but more than halves the aging rate over
632 the polar regions (Figs. 11 and 12). This is because faster BC aging over non-polar
633 regions reduces the amount of hydrophobic BC transported to remote areas. However, the
634 absolute aging rate over the polar regions is several orders of magnitude smaller than that
635 in non-polar regions. Chemical oxidation aging thus has a vanishingly small (<0.5%)
636 impact on the global annual mean BC aging rate (Table 2). It leads to only a small (<1%)
637 reduction in BC column burden and zonal mean concentration globally (Figs. 13 and 14)
638 as well as global BC lifetime (Table 2). Croft et al. (2005) showed a comparably small
639 (~5%) decrease in global BC burden and lifetime when the chemical oxidation process is
640 included, while Huang et al. (2013) found a ~10% decrease in BC burden and lifetime
641 with the incorporation of chemical oxidation aging.

642

643 **4.2 Size distribution of hydrophobic BC**

644 Reducing the geometric mean diameter of hydrophobic BC from 60 to 30 nm (D_{BCPO30})
645 and the standard deviation from 1.8 to 1.4 ($SD_{BCPO1.4}$) increases hydrophobic BC
646 number concentration. As a result, more hydrophobic BC particles are available for
647 condensation-coagulation aging, leading to a 5–50% increase of condensation-induced
648 aging rate within 60°S–60°N below 900 hPa (Figs. S9 and S10). The enhancement of
649 aging rate is stronger for $SD_{BCPO1.4}$ than for D_{BCPO30} , suggesting that the
650 condensation-induced aging is more sensitive to the change in geometric standard

651 deviation than geometric mean diameter. Interestingly, the largest enhancement for both
652 simulations is over the oceans, while only less than 10% increase occurs in the source
653 regions. This is probably because the BC aging rate over the oceans is much smaller than
654 that over the source regions (Fig. 2), making it more sensitive to the change in the size
655 distribution of hydrophobic BC.

656

657 D_{BCPO30} increases the coagulation-induced aging rate by up to a factor of 2 within
658 60°S–60°N near the surface (Fig. S11), particularly in source regions, whereas $SD_{BCPO1.4}$
659 only increases the coagulation-induced surface-layer aging rate along shipping corridors
660 over the oceans, with up to 50% decrease in the rest of non-polar regions. In the middle
661 to upper troposphere and the polar regions, both D_{BCPO30} and $SD_{BCPO1.4}$ result in a more
662 than 50% decrease in coagulation-induced and condensation-induced BC aging rates
663 (Figs. S10 and S12), because of the reduction in the amount of hydrophobic BC
664 transported to remote regions. The change in total BC aging rate shows a very similar
665 spatial pattern with that of condensation (Figs. 11 and 12), due to the dominant role of
666 condensation-induced aging globally. However, because of the rather low BC aging rate
667 over the oceans and at high altitudes relative to that over source regions, the impact of
668 hydrophobic BC size distribution on global BC distribution is dominated by the change
669 of aging rate in source regions for both D_{BCPO30} and $SD_{BCPO1.4}$, which results in less
670 than 5% reductions in BC column burden and zonal mean concentration globally, except
671 a 10–20% reduction in the tropics at 600–200 hPa (Figs. 13 and 14). The resulting global
672 annual mean BC load and lifetime show negligible (<1%) increases (Table 2).

673

674 Increasing the geometric mean diameter of hydrophobic BC from 60 to 90 nm (D_{BCPO90})
675 and the standard deviation from 1.8 to 2.0 ($SD_{BCPO2.0}$) decreases hydrophobic BC
676 number concentration. Both simulations exhibit opposite patterns of the change in BC
677 aging rate compared with those from D_{BCPO30} and $SD_{BCPO1.4}$ (Figs. S13–18), because of

678 lower hydrophobic BC number concentrations in the former two. Nevertheless, similar to
679 $D_{\text{BCPO}30}$ and $SD_{\text{BCPO}1.4}$, $D_{\text{BCPO}90}$ and $SD_{\text{BCPO}2.0}$ also result in less than 10% change in
680 global BC column burden and zonal mean concentration (Figs. S19–20). We note that the
681 observationally constrained accumulation mode BC mass size distributions for HIPPO
682 have a geometric mean diameter of ~ 180 nm (Schwarz et al., 2010), which is the upper
683 bound value used in this study for the geometric mean diameter of mass size distribution
684 (~ 60 – 180 nm) converted from that of number size distribution (30–90 nm).

685

686 **4.3 Size distribution of hydrophilic aerosols**

687 Increasing the geometric mean diameters of all hydrophilic aerosols by 50% ($D_{\text{PI}+50\%}$)
688 and the standard deviations by 0.2 ($SD_{\text{PI}+0.2}$) reduces the number concentration of
689 hydrophilic particles. This results in an enhanced condensation-induced aging rate due to
690 fewer hydrophilic particles competing for condensed soluble materials, but a reduced
691 coagulation-induced aging rate due to fewer hydrophilic particles available for
692 coagulating with hydrophobic BC. Both simulations show up to 50% increase in the
693 annual mean condensation-induced BC aging rate at 60°S – 60°N below 900 hPa (Figs.
694 S9–10), particularly over the oceans where BC aging rate is relatively small. The faster
695 aging through condensation in the lower troposphere reduces the amount of hydrophobic
696 BC transported to higher altitudes and the polar regions, resulting in more than 50%
697 slower condensation-induced aging in remote regions. In contrast, the
698 coagulation-induced aging rate decreases globally, by 20–50% at 60°S – 60°N near the
699 surface and more than 50% in elsewhere (Figs. S11 and S12). The change of total BC
700 aging rate follows the spatial pattern of the condensation-induced aging rate (Figs. 11 and
701 12). The global annual mean BC aging rate is slightly higher ($\sim 1.5\%$) in both $D_{\text{PI}+50}$ and
702 $SD_{\text{PI}+0.2}$. Figures 11 and 12 show that increasing geometric mean diameters and standard
703 deviations of hydrophilic particles only reduces global BC column burden and zonal
704 mean concentration by less than 10% and BC lifetime by less than 1% (Table 2).

705

706 Decreasing the geometric mean diameters of hydrophilic aerosols by 50% ($D_{PI-50\%}$) and
707 the standard deviations by 0.2 ($SD_{PI-0.2}$) increases the number concentration of
708 hydrophilic particles, resulting in an opposite spatial pattern of the change in BC aging
709 rate (Figs. S13–18) than that from D_{PI+50} and $SD_{PI+0.2}$. Both condensation-induced and
710 coagulation-induced aging rates are more sensitive to the decrease of geometric mean
711 diameters ($D_{PI-50\%}$) than geometric standard deviations ($SD_{PI-0.2}$) globally. The
712 resulting BC concentration change is less than 10% over much of the globe, with a <2%
713 increase in global BC load and lifetime (Table 2).

714

715 **4.4 Condensation threshold**

716 The condensation-induced BC aging rate is critically dependent on the condensation
717 threshold β (see Eq. (9)), which represents the mass fraction of condensed soluble
718 materials on hydrophobic BC required for hydrophobic-to-hydrophilic BC conversion.
719 Reducing β by a factor of 2 (BETA2.5) increases the condensation-induced aging rate by
720 5–10% near source regions and by up to 50% over remote oceans at 60°S–60°N (Fig. S9),
721 while the condensation-induced aging rate decreases by 20–50% in the middle and upper
722 troposphere and more than 80% over the polar regions (Fig. S10), because of the reduced
723 amount of hydrophobic BC transported to remote areas. The change in total BC aging
724 rate follows the pattern of the change in condensation-induced aging rate, with major
725 increases at 60°S–60°N below 900 hPa (Figs. 11 and 12). This results in a decrease
726 (<20%) of BC concentration globally, particularly in the tropics at 600–200 hPa (Figs. 13
727 and 14). In contrast, doubling β (BETA10) shows the opposite spatial pattern of the
728 change in BC aging rate compared with BETA2.5 (Figs. S13 and S14), where the aging
729 rate decreases by up to 20% in the non-polar regions below 900 hPa but increases by up
730 to more than twofold at high altitudes and polar regions. The resulting global BC load
731 and lifetime, however, change by less than 2% for both BETA10 and BETA2.5 (Table 2).

732

733 There is strong spatial heterogeneity in the sensitivity of microphysical BC aging to
734 aerosol size distribution, condensation threshold, and chemical oxidation, with little
735 sensitivity over the source regions but rather large sensitivity in remote regions. However,
736 the BC aging rate in remote areas is several orders of magnitude smaller than that over
737 source regions. As a result, the global BC column burden and zonal mean concentration
738 are only slightly affected by the change in the above-mentioned factors, with less than 5%
739 change over much of the globe (Figs. 13 and 14). Very small changes are also seen in
740 global BC lifetime (Table 2). Nevertheless, using a uniform aerosol size distribution and
741 condensation threshold may not be realistic or representative, particularly on a regional
742 scale with complex atmospheric conditions. The two-/three-moment aerosol scheme (e.g.,
743 Li et al., 2008), which predicts aerosol size distribution from simulated aerosol mass,
744 number, and/or surface area depending on atmospheric conditions, could be a potential
745 improvement to represent and understand BC aging, interaction with cloud, and
746 deposition compared with the microphysical scheme developed in this study.

747

748 **5. Conclusions**

749 We have developed and examined a microphysics-based BC aging scheme that explicitly
750 accounts for condensation and coagulation processes in GEOS-Chem global CTM. We
751 analyzed the difference in BC aging rate between the microphysics-based scheme and a
752 fixed aging scheme with an e-folding time of 1.2 days, followed by a systematic
753 evaluation of BC simulations using HIPPO observations from 2009 to 2011. We further
754 analyzed the effects of the microphysics-based aging scheme on global BC distribution
755 and lifetime. Finally, we quantified the uncertainty associated with aerosol size
756 distribution and condensation threshold in the microphysics-based aging scheme and the
757 impact of heterogeneous chemical oxidation on BC aging.

758

759 In the microphysics-based BC aging scheme, we converted aerosol mass to number
760 concentration by assuming lognormal aerosol size distributions. We computed the
761 condensation-induced aging rate from the condensation of soluble materials onto
762 hydrophobic BC, which converted hydrophobic to hydrophilic BC when the condensed
763 mass reached the condensation threshold (β in Eq. (9)). We computed the
764 coagulation-induced aging rate from the coagulation between hydrophobic BC and
765 hydrophilic particles, assuming a hydrophobic-to-hydrophilic BC conversion upon
766 coagulating. This microphysics-based scheme thus incorporated an explicit microphysical
767 representation of BC aging and retained the computational efficiency of the fixed aging
768 scheme. The microphysical aging scheme can also be applied in other CTMs.

769

770 The microphysical aging rate was a factor of 2–6 higher than that from the fixed aging
771 scheme in the lower troposphere over such source regions as East China, India, Europe,
772 United States, tropical continents, and marine shipping corridors, because of strong
773 emissions of sulfate-nitrate and SOA precursors, which resulted in faster BC aging
774 through condensation and coagulation. The microphysical aging rate is more than
775 fivefold lower than that from the fixed aging scheme in remote regions, where
776 condensation and coagulation are rather weak. We found that condensation dominated
777 (>70%) BC aging globally, particularly in the Southern Hemisphere and above 5 km,
778 while the largest coagulation contribution (~30%) was over East China, India, and
779 Central Africa, primarily because the hydrophilic aerosols required for coagulation were
780 substantially removed by wet scavenging during transport to remote regions.

781

782 Compared with the fixed aging scheme, the microphysical scheme substantially reduced
783 the discrepancy between modeled and observed probability density functions of BC
784 concentrations during HIPPO, particularly at BC concentrations of $< 1 \text{ ng kg}^{-1}$ and 10–50
785 ng kg^{-1} . Model results using the fixed aging scheme overestimated BC median vertical

786 profiles in the northern extratropics by ~5 times on average, while the microphysical
787 scheme improved the modeled BC vertical profiles by a factor of 2–3 throughout the
788 troposphere, particularly at 900–300 hPa. Model results using the microphysical aging
789 scheme reproduced the observed BC vertical distribution in the tropics. In the Southern
790 Hemisphere, the microphysical aging scheme reduced the model bias in BC vertical
791 profiles by a factor of 2–4, with largest improvements at 600–200 hPa, compared with the
792 fixed aging scheme. The model bias in latitudinal BC column burden along the HIPPO
793 flight tracks was reduced from +194% for the fixed aging scheme to +60% for the
794 microphysics-based scheme, with largest improvements in the tropics. The remaining
795 model-observation discrepancy for the microphysics-based simulation was likely due to
796 the uncertainty associated with BC emissions, wet scavenging, and meteorological fields
797 in the model. We note that it is also very important to evaluate BC simulations from other
798 perspectives in addition to atmospheric concentration, such as aerosol optical depth, a
799 subject requiring further investigation.

800

801 We found that the faster BC aging over the source regions from the microphysics-based
802 scheme dominated the aging effects on global BC distribution, resulting in a much lower
803 BC column burden and zonal mean concentration globally, compared with the fixed
804 aging scheme. The global annual mean BC lifetime was 4.2 days in the
805 microphysics-based scheme, where wet scavenging accounts for 80.3% of global BC
806 deposition. The resulting global BC burden was 0.25 mg m^{-2} , with 7.3% of the burden
807 above 5 km. The relatively low BC load at high altitudes had important implications on
808 the estimate of global BC radiative effects.

809

810 Furthermore, we found that BC aging rate was insensitive (<10% change) to aerosol size
811 distribution, condensation threshold, and chemical oxidation over source regions, while it
812 was the opposite (more than twofold change) in the polar regions and at high altitudes.

813 However, the BC aging rate in remote regions was orders of magnitude lower than that in
814 source regions. Thus, the global BC burden and lifetime showed little sensitivity (<5%
815 change) to the above-mentioned three factors. Nevertheless, assuming global uniform
816 aerosol size distribution and condensation threshold may not be representative or accurate,
817 particularly for regions with complex atmospheric conditions. Further improvements
818 require the incorporation of a dynamic size-resolved microphysical aging scheme.

819

820

821 **Acknowledgements**

822 This work is funded by NASA grants NNX09AF07G and NNX08AF64G from the
823 Atmospheric Chemistry Modeling and Analysis Program (ACMAP) and by the NSF
824 grants AGS-0946315 and AGS-1523296. We acknowledge the free use of HIPPO data.
825 We thank all the contributors during the HIPPO campaigns and all the contributors to the
826 development of PKU-BC inventory. We thank Rong Wang, Fangqun Yu, Peter Adams,
827 David Fahey, and Jiachen Zhang for helpful discussions.

828

829 **References**

830 Akagi, S. K., Craven, J. S., Taylor, J. W., McMeeking, G. R., Yokelson, R. J., Burling, I. R., Urbanski,
831 S. P., Wold, C. E., Seinfeld, J. H., Coe, H., Alvarado, M. J., and Weise, D. R.: Evolution of trace
832 gases and particles emitted by a chaparral fire in California, *Atmos. Chem. Phys.*, 12, 1397-1421,
833 doi:10.5194/acp-12-1397-2012, 2012.

834 Alexander, B., Park, R. J., Jacob, D. J., Li, Q. B., Yantosca, R. M., Savarino, J., Lee, C. C. W., and
835 Thiemens, M. H.: Sulfate formation in sea-salt aerosols: Constraints from oxygen isotopes, *J.*
836 *Geophys. Res.-Atmos.*, 110, D10307, doi:10.1029/2004jd005659, 2005.

837 Aquila, V., Hendricks, J., Lauer, A., Riemer, N., Vogel, H., Baumgardner, D., Minikin, A., Petzold, A.,
838 Schwarz, J. P., Spackman, J. R., Weinzierl, B., Righi, M., and Dall'Amico, M.: MADE-in: a new
839 aerosol microphysics submodel for global simulation of insoluble particles and their mixing state,

840 Geosci. Model Dev., 4, 325–355, doi:10.5194/gmd-4-325-2011, 2011.

841 Bond, T. C., Habib, G., and Bergstrom, R. W.: Limitations in the enhancement of visible light
842 absorption due to mixing state, *J. Geophys. Res.-Atmos.*, 111, D20211,
843 doi:10.1029/2006jd007315, 2006.

844 Bond, T. C., Bhardwaj, E., Dong, R., Jogani, R., Jung, S. K., Roden, C., Streets, D. G., and Trautmann,
845 N. M.: Historical emissions of black and organic carbon aerosol from energy-related combustion,
846 1850-2000, *Global Biogeochem. Cy.*, 21, Gb2018, doi:10.1029/2006gb002840, 2007.

847 Bond, T. C., Doherty, S. J., Fahey, D. W., Forster, P. M., Bernsten, T., DeAngelo, B. J., Flanner, M. G.,
848 Ghan, S., Karcher, B., Koch, D., Kinne, S., Kondo, Y., Quinn, P. K., Sarofim, M. C., Schultz, M.
849 G., Schulz, M., Venkataraman, C., Zhang, H., Zhang, S., Bellouin, N., Guttikunda, S. K., Hopke,
850 P. K., Jacobson, M. Z., Kaiser, J. W., Klimont, Z., Lohmann, U., Schwarz, J. P., Shindell, D.,
851 Storelvmo, T., Warren, S. G., and Zender, C. S.: Bounding the role of black carbon in the climate
852 system: A scientific assessment, *J. Geophys. Res.-Atmos.*, 118, 5380-5552,
853 doi:10.1002/jgrd.50171, 2013.

854 Chung, S. H. and Seinfeld, J. H.: Global distribution and climate forcing of carbonaceous aerosols, *J.*
855 *Geophys. Res.-Atmos.*, 107, 4407, doi:10.1029/2001JD001397, 2002.

856 Cooke, W. F., Liousse, C., Cachier, H., and Feichter, J.: Construction of a 1 degrees x 1 degrees fossil
857 fuel emission data set for carbonaceous aerosol and implementation and radiative impact in the
858 ECHAM4 model, *J. Geophys. Res.-Atmos.*, 104, 22137–22162, doi:10.1029/1999jd900187,
859 1999.

860 Cozic, J., Mertes, S., Verheggen, B., Cziczo, D. J., Gallavardin, S. J., Walter, S., Baltensperger, U., and
861 Weingartner, E.: Black carbon enrichment in atmospheric ice particle residuals observed in lower
862 tropospheric mixed phase clouds, *J. Geophys. Res.-Atmos.*, 113, D15209,
863 doi:10.1029/2007jd009266, 2008.

864 Croft, B., Lohmann, U., and von Salzen, K.: Black carbon ageing in the Canadian Centre for Climate
865 modelling and analysis atmospheric general circulation model, *Atmos. Chem. Phys.*, 5,
866 1931–1949, doi:10.5194/acp-5-1931-2005, 2005.

867 Dahneke, B.: Simple kinetic theory of Brownian diffusion in vapors and aerosols, in Theory of
868 Dispersed Multiphase Flow, R. E. Meyer, ed., Academic Press, New York, 97-133, 1983.

869 Decesari, S., Facchini, M. C., Matta, E., Mircea, M., Fuzzi, S., Chughtai, A. R., and Smith, D. M.:
870 Water soluble organic compounds formed by oxidation of soot, *Atmos. Environ.*, 36, 1827-1832,
871 doi:10.1016/S1352-2310(02)00141-3, 2002.

872 Dentener, F., Kinne, S., Bond, T., Boucher, O., Cofala, J., Generoso, S., Ginoux, P., Gong, S.,
873 Hoelzemann, J. J., Ito, A., Marelli, L., Penner, J. E., Putaud, J.-P., Textor, C., Schulz, M., van der
874 Werf, G. R., and Wilson, J.: Emissions of primary aerosol and precursor gases in the years 2000
875 and 1750 prescribed datasets for AeroCom, *Atmos. Chem. Phys.*, 6, 4321-4344,
876 doi:10.5194/acp-6-4321-2006, 2006.

877 Fairlie, T. D., Jacob, D. J., and Park, R. J.: The impact of transpacific transport of mineral dust in the
878 United States, *Atmos. Environ.*, 41, 1251-1266, doi:10.1016/j.atmosenv.2006.09.048, 2007.

879 Friedman, B., Kulkarni, G., Beranek, J., Zelenyuk, A., Thornton, J. A., and Cziczo, D. J.: Ice
880 nucleation and droplet formation by bare and coated soot particles, *J. Geophys. Res.-Atmos.*, 116,
881 D17203, doi:10.1029/2011jd015999, 2011.

882 Guenther, A., Karl, T., Harley, P., Wiedinmyer, C., Palmer, P. I., and Geron, C.: Estimates of global
883 terrestrial isoprene emissions using MEGAN (Model of Emissions of Gases and Aerosols from
884 Nature), *Atmos. Chem. Phys.*, 6, 3181-3210, 2006.

885 Granier, C., Bessagnet, B., Bond, T., D'Angiola, A., van der Gon, H. D., Frost, G. J., Heil, A., Kaiser, J.
886 W., Kinne, S., Klimont, Z., Kloster, S., Lamarque, J. F., Liousse, C., Masui, T., Meleux, F.,
887 Mieville, A., Ohara, T., Raut, J. C., Riahi, K., Schultz, M. G., Smith, S. J., Thompson, A., van
888 Aardenne, J., van der Werf, G. R., and van Vuuren, D. P.: Evolution of anthropogenic and
889 biomass burning emissions of air pollutants at global and regional scales during the 1980-2010
890 period, *Climatic Change*, 109, 163-190, doi:10.1007/s10584-011-0154-1, 2011.

891 He, C., Li, Q. B., Liou, K. N., Zhang, J., Qi, L., Mao, Y., Gao, M., Lu, Z., Streets, D. G., Zhang, Q.,
892 Sarin, M. M., and Ram, K.: A global 3-D CTM evaluation of black carbon in the Tibetan Plateau,
893 *Atmos. Chem. Phys.*, 14, 7091-7112, doi:10.5194/acp-14-7091-2014, 2014a.

894 He, C., Li, Q. B., Liou, K. N., Takano, Y., Gu, Y., Qi, L., Mao, Y. H., and Leung, L. R.: Black carbon
895 radiative forcing over the Tibetan Plateau, *Geophys. Res. Lett.*, 41, 7806-7813,
896 doi:10.1002/2014gl062191, 2014b.

897 He, C., Liou, K.-N., Takano, Y., Zhang, R., Levy Zamora, M., Yang, P., Li, Q., and Leung, L. R.:
898 Variation of the radiative properties during black carbon aging: theoretical and experimental
899 intercomparison, *Atmos. Chem. Phys.*, 15, 11967-11980, doi:10.5194/acp-15-11967-2015, 2015.

900 Huang, Y., Wu, S., Dubey, M. K., and French, N. H. F.: Impact of aging mechanism on model
901 simulated carbonaceous aerosols, *Atmos. Chem. Phys.*, 13, 6329-6343,
902 doi:10.5194/acp-13-6329-2013, 2013.

903 Jacobson, M. Z.: Short-term effects of controlling fossil-fuel soot, biofuel soot and gases, and methane
904 on climate, Arctic ice, and air pollution health, *J. Geophys. Res.-Atmos.*, 115, D14209,
905 doi:10.1029/2009jd013795, 2010.

906 Jacobson, M. Z.: Effects of biomass burning on climate, accounting for heat and moisture fluxes,
907 black and brown carbon, and cloud absorption effects, *J. Geophys. Res. Atmos.*, 119, 8980-9002,
908 doi:10.1002/2014JD021861, 2014.

909 Johnson, K. S., Zuberi, B., Molina, L. T., Molina, M. J., Iedema, M. J., Cowin, J. P., Gaspar, D. J.,
910 Wang, C., and Laskin, A.: Processing of soot in an urban environment: case study from the
911 Mexico City Metropolitan Area, *Atmos. Chem. Phys.*, 5, 3033-3043, 2005.

912 Khalizov, A. F., Cruz-Quinones, M., and Zhang, R. Y.: Heterogeneous Reaction of NO₂ on Fresh and
913 Coated Soot Surfaces, *J. Phys. Chem. A*, 114, 7516-7524, doi:10.1021/Jp1021938, 2010.

914 Koch, D., Schulz, M., Kinne, S., McNaughton, C., Spackman, J. R., Balkanski, Y., Bauer, S., Berntsen,
915 T., Bond, T. C., Boucher, O., Chin, M., Clarke, A., De Luca, N., Dentener, F., Diehl, T., Dubovik,
916 O., Easter, R., Fahey, D. W., Feichter, J., Fillmore, D., Freitag, S., Ghan, S., Ginoux, P., Gong, S.,
917 Horowitz, L., Iversen, T., Kirkevåg, A., Klimont, Z., Kondo, Y., Krol, M., Liu, X., Miller, R.,
918 Montanaro, V., Moteki, N., Myhre, G., Penner, J. E., Perlwitz, J., Pitari, G., Reddy, S., Sahu, L.,
919 Sakamoto, H., Schuster, G., Schwarz, J. P., Seland, O., Stier, P., Takegawa, N., Takemura, T.,
920 Textor, C., van Aardenne, J. A., and Zhao, Y.: Evaluation of black carbon estimations in global

921 aerosol models, *Atmos. Chem. Phys.*, 9, 9001-9026, 2009.

922 Koepke, P., Hess, M., Schult, I., and Shettle, E. P.: Global Aerosol Data Set, Report No. 243,
923 Max-Planck-Institut für Meteorologie, Hamburg, ISSN 0937-1060, 1997.

924 Kondo, Y., Sahu, L., Moteki, N., Khan, F., Takegawa, N., Liu, X., Koike, M., and Miyakawa, T.:
925 Consistency and traceability of black carbon measurements made by laser-induced incandescence,
926 thermal-optical transmittance, and filter-based photo-absorption techniques, *Aero. Sci. Technol.*,
927 45, 295-312, 2011.

928 Lamarque, J. F., Bond, T. C., Eyring, V., Granier, C., Heil, A., Klimont, Z., Lee, D., Liousse, C.,
929 Mieville, A., Owen, B., Schultz, M. G., Shindell, D., Smith, S. J., Stehfest, E., Van Aardenne, J.,
930 Cooper, O. R., Kainuma, M., Mahowald, N., McConnell, J. R., Naik, V., Riahi, K., and van
931 Vuuren, D. P.: Historical (1850-2000) gridded anthropogenic and biomass burning emissions of
932 reactive gases and aerosols: methodology and application, *Atmos. Chem. Phys.*, 10, 7017-7039,
933 2010.

934 Lana, A., Bell, T. G., Simo, R., Vallina, S. M., Ballabrera-Poy, J., Kettle, A. J., Dachs, J., Bopp, L.,
935 Saltzman, E. S., Stefels, J., Johnson, J. E., and Liss, P. S.: An updated climatology of surface
936 dimethylsulfide concentrations and emission fluxes in the global ocean, *Global Biogeochem. Cy.*,
937 25, Gb1004, doi:10.1029/2010gb003850, 2011.

938 Li, G. H., Wang, Y., and Zhang, R. Y.: Implementation of a two-moment bulk microphysics scheme to
939 the WRF model to investigate aerosol-cloud interaction, *J. Geophys. Res.-Atmos.*, 113, D15211,
940 doi:10.1029/2007jd009361, 2008.

941 Li, K., Liao, H., Mao, Y., and Ridley, D. A.: Source sector and region contributions to concentration
942 and direct radiative forcing of black carbon in China, *Atmos. Environ.*,
943 doi:10.1016/j.atmosenv.2015.06.014, 2015.

944 Liao, H., Henze, D. K., Seinfeld, J. H., Wu, S. L., and Mickley, L. J.: Biogenic secondary organic
945 aerosol over the United States: Comparison of climatological simulations with observations, *J.*
946 *Geophys. Res.-Atmos.*, 112, D06201, doi:10.1029/2006jd007813, 2007.

947 Liou, K. N., Takano, Y., He, C., Yang, P., Leung, L. R., Gu, Y., and Lee, W. L.: Stochastic

948 parameterization for light absorption by internally mixed BC/dust in snow grains for application
949 to climate models, *J. Geophys. Res.-Atmos.*, 119, 7616-7632, doi:10.1002/2014jd021665, 2014.

950 Liu, H. Y., Jacob, D. J., Bey, I., and Yantosca, R. M.: Constraints from Pb-210 and Be-7 on wet
951 deposition and transport in a global three-dimensional chemical tracer model driven by
952 assimilated meteorological fields, *J. Geophys. Res.-Atmos.*, 106, 12109–12128,
953 doi:10.1029/2000jd900839, 2001.

954 Liu, J. F., Fan, S. M., Horowitz, L. W., and Levy, H.: Evaluation of factors controlling long-range
955 transport of black carbon to the Arctic, *J. Geophys. Res.-Atmos.*, 116, D04307,
956 doi:10.1029/2010jd015145, 2011.

957 Liu, X. H., Penner, J. E., and Wang, M. H.: Influence of anthropogenic sulfate and black carbon on
958 upper tropospheric clouds in the NCAR CAM3 model coupled to the IMPACT global aerosol
959 model, *J. Geophys. Res.-Atmos.*, 114, D03204, doi:10.1029/2008jd010492, 2009.

960 Moffet, R. C., and Prather, K. A.: In-situ measurements of the mixing state and optical properties of
961 soot with implications for radiative forcing estimates, *P. Natl. Acad. Sci. USA*, 106, 11872-11877,
962 doi:10.1073/pnas.0900040106, 2009.

963 Molod, A., Takacs, L., Suarez, M., Bacmeister, J., Song, I.-S., and Eichmann, A.: The GEOS-5
964 Atmospheric General Circulation Model: Mean Climate and Development from MERRA to
965 Fortuna. NASA Technical Report Series on Global Modeling and Data Assimilation, NASA
966 TM—2012-104606, Vol. 28, 117 pp, 2012.

967 Moteki, N., Kondo, Y., Miyazaki, Y., Takegawa, N., Komazaki, Y., Kurata, G., Shirai, T., Blake, D. R.,
968 Miyakawa, T., and Koike, M.: Evolution of mixing state of black carbon particles: Aircraft
969 measurements over the western Pacific in March 2004, *Geophys. Res. Lett.*, 34, L11803,
970 doi:10.1029/2006gl028943, 2007.

971 Oshima, N., and Koike, M.: Development of a parameterization of black carbon aging for use in
972 general circulation models, *Geosci. Model Dev.*, 6, 263-282, doi:10.5194/gmd-6-263-2013, 2013.

973 Park, R. J., Jacob, D. J., Chin, M., and Martin, R. V.: Sources of carbonaceous aerosols over the
974 United States and implications for natural visibility, *J. Geophys. Res.-Atmos.*, 108, 4355,

975 doi:10.1029/2002jd003190, 2003.

976 Park, R. J., Jacob, D. J., Field, B. D., Yantosca, R. M., and Chin, M.: Natural and transboundary
977 pollution influences on sulfate-nitrate-ammonium aerosols in the United States: Implications for
978 policy, *J. Geophys. Res.-Atmos.*, 109, D15204, doi:10.1029/2003jd004473, 2004.

979 Park, R. J., Jacob, D. J., Palmer, P. I., Clarke, A. D., Weber, R. J., Zondlo, M. A., Eisele, F. L., Bandy,
980 A. R., Thornton, D. C., Sachse, G. W., and Bond, T. C.: Export efficiency of black carbon aerosol
981 in continental outflow: Global implications, *J. Geophys. Res.-Atmos.*, 110, D11205,
982 doi:10.1029/2004jd005432, 2005.

983 Painter, T. H., Flanner, M. G., Kaser, G., Marzeion, B., VanCuren, R. A., and Abdalati, W.: End of the
984 Little Ice Age in the Alps forced by industrial black carbon, *P. Natl. Acad. Sci. USA*, 110,
985 15216-15221, doi:10.1073/pnas.1302570110, 2013.

986 Pöschl, U., Letzel, T., Schauer, C., and Niessner, R.: Interaction of ozone and water vapor with spark
987 discharge soot aerosol particles coated with benzo[a]pyrene: O₃ and H₂O adsorption,
988 benzo[a]pyrene degradation, and atmospheric implications, *J. Phys. Chem. A*, 105, 4029–4041,
989 doi:10.1021/jp004137n, 2001.

990 Prenni, A. J., Petters, M. D., Kreidenweis, S. M., DeMott, P. J., and Ziemann, P. J.: Cloud droplet
991 activation of secondary organic aerosol, *J. Geophys. Res.-Atmos.*, 112, D10223,
992 doi:10.1029/2006jd007963, 2007.

993 Ramanathan, V. and Carmichael, G.: Global and regional climate changes due to black carbon, *Nat.*
994 *Geosci.*, 1, 221–227, doi:10.1038/ngeo156, 2008.

995 Randerson, J. T., Chen, Y., van der Werf, G. R., Rogers, B. M., and Morton, D. C.: Global burned area
996 and biomass burning emissions from small fires, *J. Geophys. Res.-Biogeo.*, 117, G04012,
997 doi:10.1029/2012jg002128, 2012.

998 Riemer, N., Vogel, H., and Vogel, B.: Soot aging time scales in polluted regions during day and night,
999 *Atmos. Chem. Phys.*, 4, 1885–1893, doi:10.5194/acp-4-1885-2004, 2004.

1000 Samset, B. H., Myhre, G., Schulz, M., Balkanski, Y., Bauer, S., Berntsen, T. K., Bian, H., Bellouin, N.,
1001 Diehl, T., Easter, R. C., Ghan, S. J., Iversen, T., Kinne, S., Kirkevåg, A., Lamarque, J. F., Lin, G.,

1002 Liu, X., Penner, J. E., Seland, O., Skeie, R. B., Stier, P., Takemura, T., Tsigaridis, K., and Zhang,
1003 K.: Black carbon vertical profiles strongly affect its radiative forcing uncertainty, *Atmos. Chem.*
1004 *Phys.*, 13, 2423-2434, doi:10.5194/acp-13-2423-2013, 2013.

1005 Scarnato, B. V., Vahidinia, S., Richard, D. T., and Kirchstetter, T. W.: Effects of internal mixing and
1006 aggregate morphology on optical properties of black carbon using a discrete dipole
1007 approximation model, *Atmos. Chem. Phys.*, 13, 5089-5101, doi:10.5194/acp-13-5089-2013,
1008 2013.

1009 Schwarz, J. P., Gao, R. S., Spackman, J. R., Watts, L. A., Thomson, D. S., Fahey, D. W., Ryerson, T. B.,
1010 Peischl, J., Holloway, J. S., Trainer, M., Frost, G. J., Baynard, T., Lack, D. A., de Gouw, J. A.,
1011 Warneke, C., and Del Negro, L. A.: Measurement of the mixing state, mass, and optical size of
1012 individual black carbon particles in urban and biomass burning emissions, *Geophys. Res. Lett.*,
1013 35, L13810, doi:10.1029/2008gl033968, 2008.

1014 Schwarz, J. P., Spackman, J. R., Gao, R. S., Watts, L. A., Stier, P., Schulz, M., Davis, S. M., Wofsy, S.
1015 C., and Fahey, D. W.: Global-scale black carbon profiles observed in the remote atmosphere and
1016 compared to models, *Geophys. Res. Lett.*, 37, L18812, doi:10.1029/2010gl044372, 2010.

1017 Schwarz, J. P., Samset, B. H., Perring, A. E., Spackman, J. R., Gao, R. S., Stier, P., Schulz, M., Moore,
1018 F. L., Ray, E. A., and Fahey, D. W.: Global-scale seasonally resolved black carbon vertical
1019 profiles over the Pacific, *Geophys. Res. Lett.*, 40, 5542-5547, doi:10.1002/2013gl057775, 2013.

1020 Seinfeld, J. H., and S. N. Pandis, *Atmospheric Chemistry and Physics, From Air Pollution to Climate*
1021 *Change*, 2nd ed., John Wiley, Hoboken, N. J., 400–610, 2006.

1022 Shen, Z., Liu, J., Horowitz, L. W., Henze, D. K., Fan, S., H., Levy II, Mauzerall, D. L., Lin, J.-T., and
1023 Tao, S.: Analysis of transpacific transport of black carbon during HIPPO-3: implications for
1024 black carbon aging, *Atmos. Chem. Phys.*, 14, 6315-6327, doi:10.5194/acp-14-6315-2014, 2014.

1025 Schulz, M., Textor, C., Kinne, S., Balkanski, Y., Bauer, S., Bernsten, T., Berglen, T., Boucher, O.,
1026 Dentener, F., Guibert, S., Isaksen, I. S. A., Iversen, T., Koch, D., Kirkevåg, A., Liu, X.,
1027 Montanaro, V., Myhre, G., Penner, J. E., Pitari, G., Reddy, S., Seland, O., Stier, P., and Takemura,
1028 T.: Radiative forcing by aerosols as derived from the AeroCom present-day and pre-industrial

1029 simulations, *Atmos. Chem. Phys.*, 6, 5225-5246, 2006.

1030 Textor, C., Schulz, M., Guibert, S., Kinne, S., Balkanski, Y., Bauer, S., Berntsen, T., Berglen, T.,
1031 Boucher, O., Chin, M., Dentener, F., Diehl, T., Easter, R., Feichter, H., Fillmore, D., Ghan, S.,
1032 Ginoux, P., Gong, S., Grini, A., Hendricks, J., Horowitz, L., Huang, P., Isaksen, I., Iversen, I.,
1033 Kloster, S., Koch, D., Kirkevåg, A., Kristjansson, J. E., Krol, M., Lauer, A., Lamarque, J. F., Liu,
1034 X., Montanaro, V., Myhre, G., Penner, J., Pitari, G., Reddy, S., Seland, Ø., Stier, P., Takemura, T.,
1035 and Tie, X.: Analysis and quantification of the diversities of aerosol life cycles within AeroCom,
1036 *Atmos. Chem. Phys.*, 6, 1777–1813, doi:10.5194/acp-6-1777-2006, 2006.

1037 van der Werf, G. R., Randerson, J. T., Giglio, L., Collatz, G. J., Mu, M., Kasibhatla, P. S., Morton, D.
1038 C., DeFries, R. S., Jin, Y., and van Leeuwen, T. T.: Global fire emissions and the contribution of
1039 deforestation, savanna, forest, agricultural, and peat fires (1997–2009), *Atmos. Chem. Phys.*, 10,
1040 11707-11735, doi:10.5194/acp-10-11707-2010, 2010.

1041 Wang, B., and Ding, Q. H.: Global monsoon: Dominant mode of annual variation in the tropics,
1042 *Dynam. Atmos. Oceans*, 44, 165-183, doi:10.1016/j.dynatmoce.2007.05.002, 2008.

1043 Wang, R., Tao, S., Wang, W. T., Liu, J. F., Shen, H. Z., Shen, G. F., Wang, B., Liu, X. P., Li, W., Huang,
1044 Y., Zhang, Y. Y., Lu, Y., Chen, H., Chen, Y. C., Wang, C., Zhu, D., Wang, X. L., Li, B. G., Liu, W.
1045 X., and Ma, J. M.: Black Carbon Emissions in China from 1949 to 2050, *Environ. Sci. Technol.*,
1046 46, 7595–7603, doi:10.1021/Es3003684, 2012a.

1047 Wang, R., Tao, S., Shen, H. Z., Wang, X. L., Li, B. G., Shen, G. F., Wang, B., Li, W., Liu, X. P., Huang,
1048 Y., Zhang, Y. Y., Lu, Y., and Ouyang, H. L.: Global Emission of Black Carbon from Motor
1049 Vehicles from 1960 to 2006, *Environ. Sci. Technol.*, 46, 1278-1284, doi:10.1021/es2032218,
1050 2012b.

1051 Wang, R., Tao, S., Ciais, P., Shen, H. Z., Huang, Y., Chen, H., Shen, G. F., Wang, B., Li, W., Zhang, Y.
1052 Y., Lu, Y., Zhu, D., Chen, Y. C., Liu, X. P., Wang, W. T., Wang, X. L., Liu, W. X., Li, B. G., and
1053 Piao, S. L.: High-resolution mapping of combustion processes and implications for CO₂
1054 emissions, *Atmos. Chem. Phys.*, 13, 5189-5203, doi:10.5194/acp-13-5189-2013, 2013.

1055 Wang, R., Tao, S., Balkanski, Y., Ciais, P., Boucher, O., Liu, J. F., Piao, S. L., Shen, H. Z., Vuolo, M.

1056 R., Valari, M., Chen, H., Chen, Y. C., Cozic, A., Huang, Y., Li, B. G., Li, W., Shen, G. F., Wang,
1057 B., and Zhang, Y. Y.: Exposure to ambient black carbon derived from a unique inventory and
1058 high-resolution model, *P. Natl. Acad. Sci. USA.*, 111, 2459–2463, doi:10.1073/pnas.1318763111,
1059 2014b.

1060 Wang, Q., Jacob, D. J., Fisher, J. A., Mao, J., Leibensperger, E. M., Carouge, C. C., Le Sager, P.,
1061 Kondo, Y., Jimenez, J. L., Cubison, M. J., and Doherty, S. J.: Sources of carbonaceous aerosols
1062 and deposited black carbon in the Arctic in winter-spring: implications for radiative forcing,
1063 *Atmos. Chem. Phys.*, 11, 12453–12473, doi:10.5194/acp-11-12453-2011, 2011.

1064 Wang, Q. Q., Jacob, D. J., Spackman, J. R., Perring, A. E., Schwarz, J. P., Moteki, N., Marais, E. A.,
1065 Ge, C., Wang, J., and Barrett, S. R. H.: Global budget and radiative forcing of black carbon
1066 aerosol: Constraints from pole-to-pole (HIPPO) observations across the Pacific, *J. Geophys.*
1067 *Res.-Atmos.*, 119, 195-206, doi:10.1002/2013jd020824, 2014a.

1068 Wang, Y. H., Jacob, D. J., and Logan, J. A.: Global simulation of tropospheric O₃-NO_x-hydrocarbon
1069 chemistry 1. Model formulation, *J. Geophys. Res.-Atmos.*, 103, 10713–10725,
1070 doi:10.1029/98jd00158, 1998.

1071 Weingartner, E., Burtscher, H., and Baltensperger, H.: Hygroscopic properties of carbon and diesel
1072 soot particles, *Atmos. Environ.*, 31, 2311–2327, 1997.

1073 Wesely, M. L.: Parameterization of Surface Resistances to Gaseous Dry Deposition in Regional-Scale
1074 Numerical Models, *Atmos. Environ.*, 23, 1293–1304, doi:10.1016/0004-6981(89)90153-4, 1989.

1075 Willis, M. D., Healy, R. M., Riemer, N., West, M., Wang, J. M., Jeong, C.-H., Wenger, J. C., Evans, G.
1076 J., Abbatt, J. P. D., and Lee, A. K. Y.: Quantification of black carbon mixing state from traffic:
1077 implications for aerosol optical properties, *Atmos. Chem. Phys. Discuss.*, 15, 33555-33582,
1078 doi:10.5194/acpd-15-33555-2015, 2015.

1079 Wofsy, S. C., Team, H. S., Team, C. M., and Team, S.: HIAPER Pole-to-Pole Observations (HIPPO):
1080 fine-grained, global-scale measurements of climatically important atmospheric gases and
1081 aerosols, *Philos. T. R. Soc. A*, 369, 2073-2086, doi:10.1098/rsta.2010.0313, 2011.

1082 Yu, F. and Luo, G.: Simulation of particle size distribution with a global aerosol model: contribution of

1083 nucleation to aerosol and CCN number concentrations, *Atmos. Chem. Phys.*, 9, 7691–7710,
1084 doi:10.5194/acp-9-7691-2009, 2009.

1085 Zhang, J., Liu, J., Tao, S., and Ban-Weiss, G. A.: Long-range transport of black carbon to the Pacific
1086 Ocean and its dependence on aging timescale, *Atmos. Chem. Phys.*, 15, 11521-11535,
1087 doi:10.5194/acp-15-11521-2015, 2015.

1088 Zhang, R. Y., Khalizov, A. F., Pagels, J., Zhang, D., Xue, H. X., and McMurry, P. H.: Variability in
1089 morphology, hygroscopicity, and optical properties of soot aerosols during atmospheric
1090 processing, *P. Natl. Acad. Sci. USA*, 105, 10291-10296, doi:10.1073/pnas.0804860105, 2008.

1091 Zuberi, B., Johnson, K. S., Aleks, G. K., Molina, L. T., and Laskin, A.: Hydrophilic properties of aged
1092 soot, *Geophys. Res. Lett.*, 32, L01807, doi:10.1029/2004gl021496, 2005.

1093

Table 1. Key aging parameters used in GEOS-Chem simulations of BC.

Simulations	Hydrophobic ^a		Hydrophilic ^a		Condensation threshold (β) ^b
	D_p (nm)	σ_p	D_p (nm)	σ_p	
Fixed aging (FIX)	<i>e</i> -folding BC aging time $\tau_{\text{fix}} = 1.2$ days				
Standard Microphysics-based (MP_{STD})^c	$D_{BC} = 60$ $D_{OC} = 60$	$\sigma_{BC} = 1.8$ $\sigma_{OC} = 1.8$	$D_{BC} = 150$ $D_{OC} = 150$ $D_{sulf} = 150$ $D_{fss} = 200$ $D_{css} = 800$	$\sigma_{BC} = 1.8$ $\sigma_{OC} = 1.8$ $\sigma_{sulf} = 1.6$ $\sigma_{fss} = 1.5$ $\sigma_{css} = 1.8$	5% of hydrophobic BC mass
Sensitivity simulations	D _{BCPO} 30	Hydrophobic $D_{BC} = 30$ nm ^d			
	D _{BCPO} 90	Hydrophobic $D_{BC} = 90$ nm ^d			
	SD _{BCPO} 1.4	Hydrophobic $\sigma_{BC} = 1.4$ ^d			
	SD _{BCPO} 2.0	Hydrophobic $\sigma_{BC} = 2.0$ ^d			
	D _{PI} +50%	All hydrophilic particles D_p increased by 50%			
	D _{PI} -50%	All hydrophilic particles D_p decreased by 50%			
	SD _{PI} +0.2	All hydrophilic particles σ_p increased by 0.2			
	SD _{PI} -0.2	All hydrophilic particles σ_p decreased by 0.2			
	BETA2.5	$\beta = 2.5\%$			
	BETA10	$\beta = 10\%$			
	MP _{chem}	Standard microphysics-based scheme with chemical oxidation parameterization from Poschl et al. (2001)			

1095 ^a D_p and σ_p are geometric mean diameter and geometric standard deviation for particle number size
1096 distribution, respectively.

1097 ^bCondensation threshold (β in Eq. (7)) represents the mass fraction of condensed soluble materials on
1098 hydrophobic BC required for hydrophobic-to-hydrophilic BC conversion. A value of 5% is used in the
1099 standard microphysics-based scheme following Riemer et al. (2004).

1100 ^cGeometric mean diameters (D_p) and standard deviations (σ_p) are following Dentener et al. (2006) and
1101 Yu and Luo (2009) for hydrophobic and hydrophilic BC and OC, and the Global Aerosol Dataset
1102 (GADS) (Koepke et al., 1997) for sulfate-nitrate-ammonia (“sulf”), fine-mode sea salt (“fss”), and
1103 coarse-mode sea salt (“css”). SOA is treated as hydrophilic OC.

1104 ^dLower and upper bounds of geometric mean diameters (30 nm and 90 nm) and standard deviations
1105 (1.4 and 2.0) for hydrophobic BC are following Bond et al. (2006).

1106

1107 **Table 2.** GEOS-Chem simulated global annual mean BC budget.

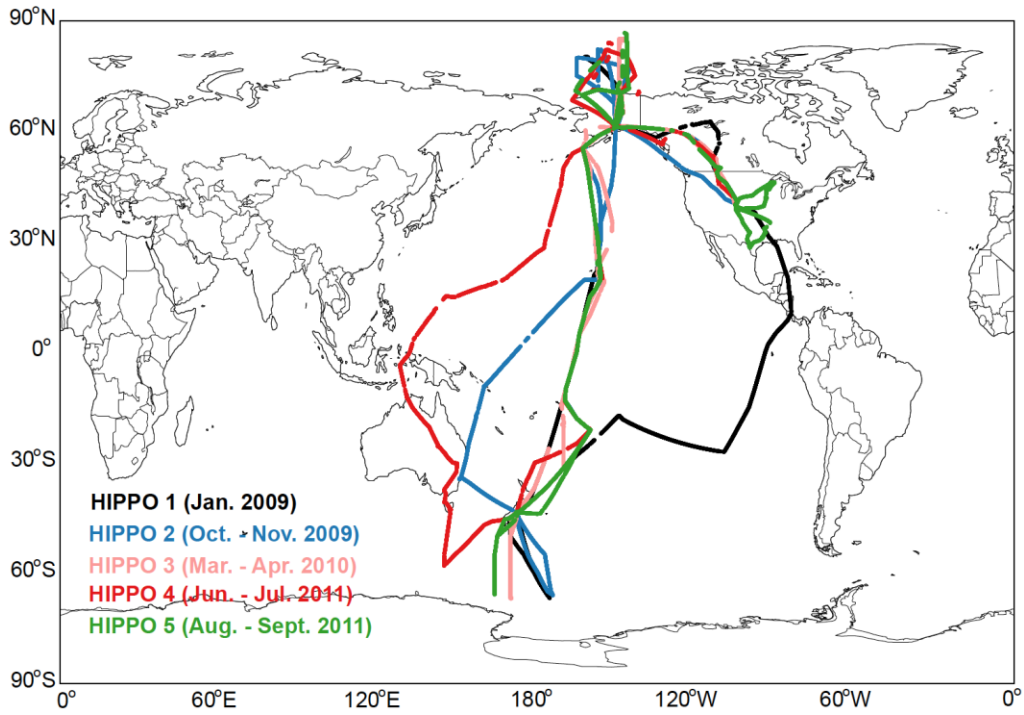
References		BC aging rate (ngC m ⁻³ h ⁻¹)			Emissions (Tg yr ⁻¹) ^c	Lifetime (day)	Loading (mg m ⁻²)	Loading above 5 km (%)	Wet deposition (%)	Hydrophilic fraction (%)
		< 5 km	> 5 km	mean						
This study	FIX	0.378	0.005	0.221	10.8	13.7	0.795	26.2	78.9	85.8
	MP _{STD}	0.560	< 0.001	0.324		4.21	0.244	7.32	80.3	98.8
	MP _{chem}	0.561		0.325		4.21	0.244	7.31	80.3	98.9
	D _{BCPO30}	0.570		0.330		4.18	0.242	7.16	80.2	99.3
	D _{BCPO90}	0.551		0.319		4.25	0.246	7.53	80.3	98.1
	SD _{BCPO1.4}	0.571		0.331		4.18	0.242	7.14	80.2	99.4
	SD _{BCPO2.0}	0.550		0.319		4.25	0.246	7.55	80.3	98.1
	D _{PI+50%}	0.568		0.329		4.19	0.243	7.19	80.3	99.2
	D _{PI-50%}	0.548		0.317		4.27	0.247	7.68	80.2	97.8
	SD _{PI+0.2}	0.567		0.328		4.19	0.243	7.20	80.3	99.2
	SD _{PI-0.2}	0.552		0.320		4.24	0.246	7.50	80.3	98.2
	BETA2.5	0.569		0.330		4.19	0.242	7.17	80.3	99.3
BETA10	0.547	0.317		4.27	0.247	7.65	80.2	97.7		
He et al. (2014a, b)		Fixed aging ($\tau = 1.2$ days)			8.1	6.6	0.29	18	83	-
Q. Q. Wang et al. (2014)		Fixed aging ($\tau = 1.2$ days)			6.5	4.2	0.15	8.7	77	-
Bond et al. (2013) ^a		Model ensemble mean			17	6.1	0.55	-	-	-
Jacobson (2012)		Aging microphysics			9.3	3.2	0.18	-	94	-
Chung et al. (2012)		Fixed aging			6.3	5.5	0.19	-	-	-
Jacobson (2010)		Aging microphysics			4.7	9.9	0.25	-	92	-
Schulz et al. (2006) ^b		Model ensemble mean			6.3	6.8±1.8	0.23±0.07	21±11	-	-

1108 ^aBased on AeroCom Phase I simulations after scaling to match AERONET BC absorption optical
 1109 depth (AAOD).

1110 ^bMean and standard deviations for eight models from AeroCom Phase I simulations. All AeroCom
 1111 models use the same emissions.

1112 ^cGlobal total BC emissions including anthropogenic and biomass burning sources.

1113



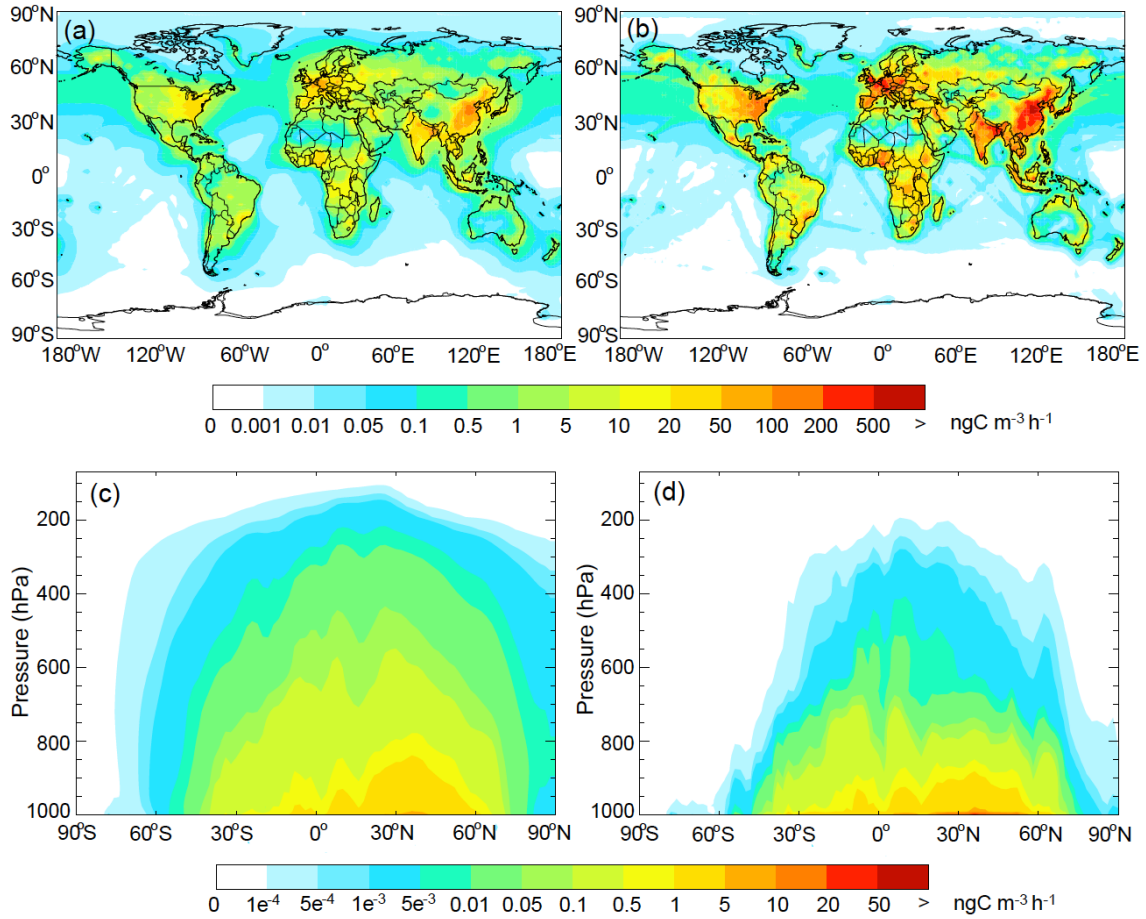
1114

1115

1116 **Figure 1.** HIPPO aircraft flight tracks in January 2009 (black), October – November
 1117 2009 (blue), March – April 2010 (pink), June – July 2011 (red), and August – September
 1118 2011 (green).

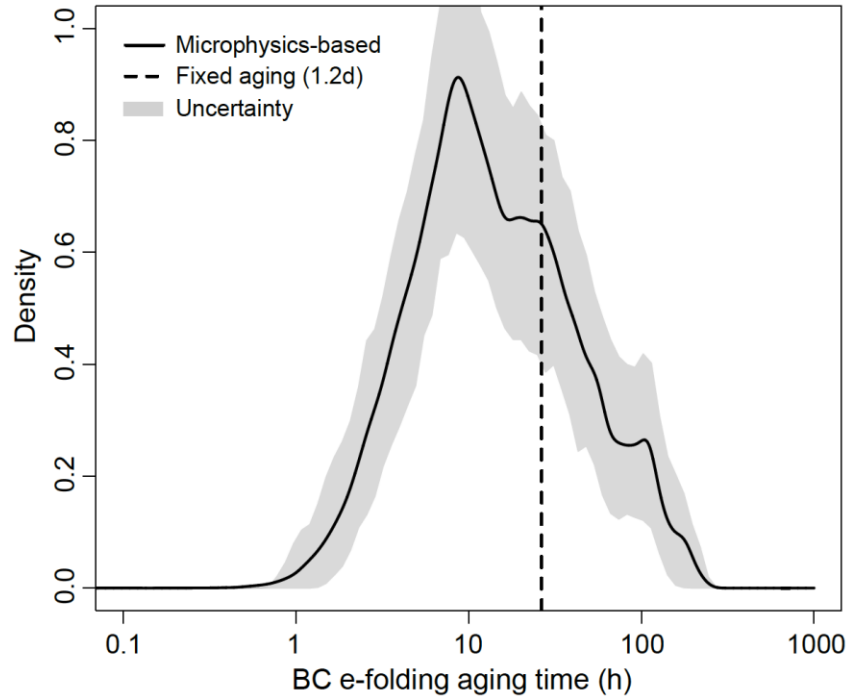
1119

1120



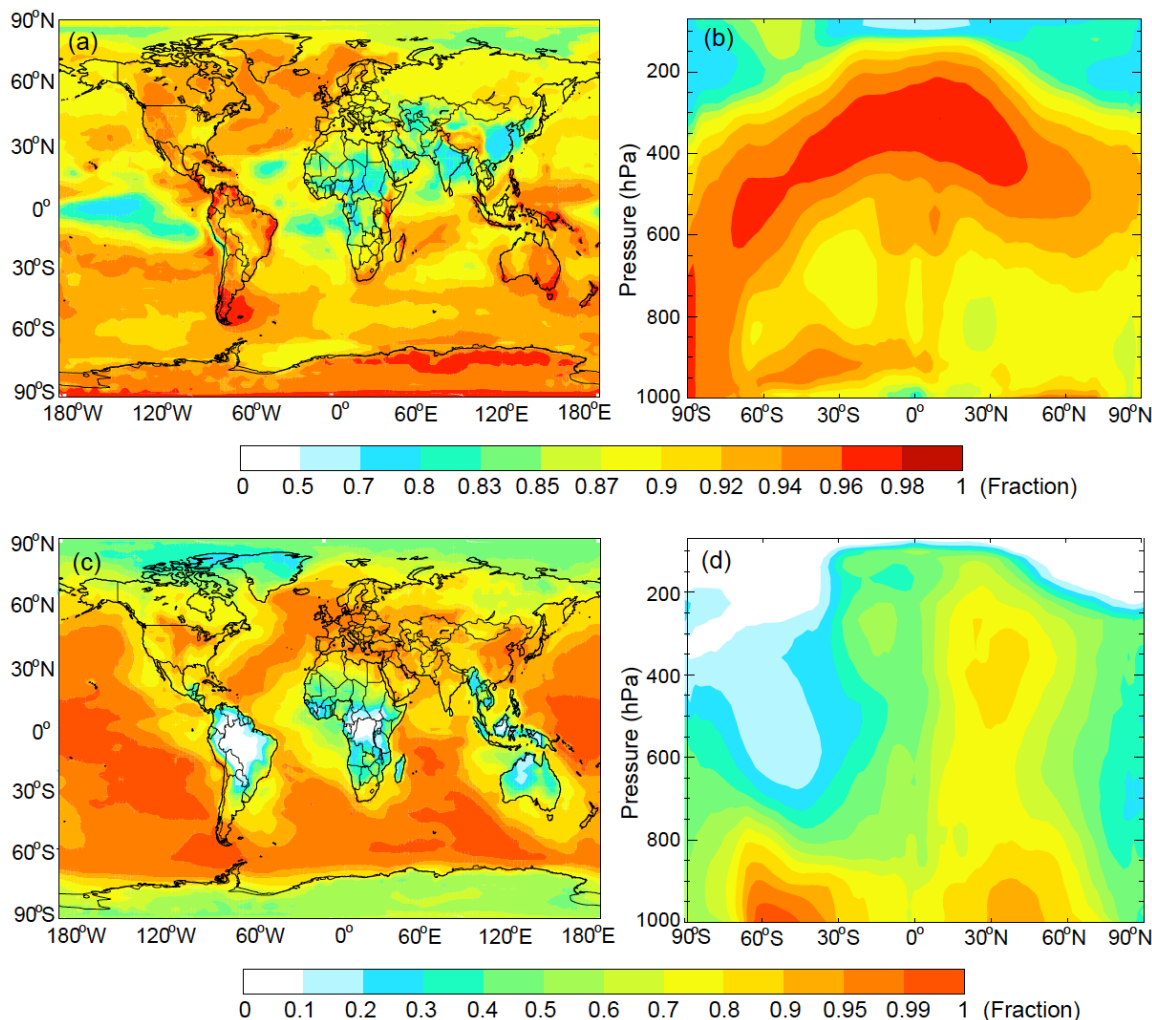
1121
 1122
 1123
 1124
 1125
 1126
 1127
 1128

Figure 2. GEOS-Chem simulated annual mean BC aging rates ($\text{ngC m}^{-3} \text{h}^{-1}$) in the surface layer (top panels) and averaged zonally (lower panels) from a fixed BC aging scheme (left panels) and a microphysics-based aging scheme (right panels). See text for details. Model results are for 2009.



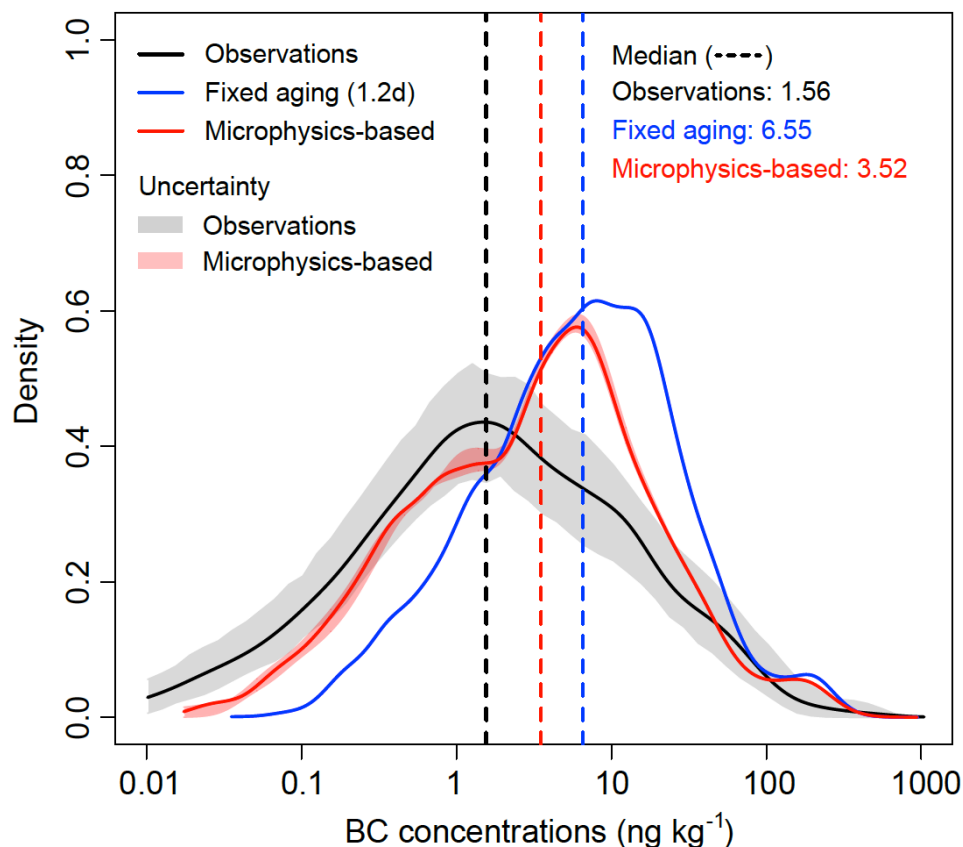
1129
 1130
 1131
 1132
 1133
 1134
 1135

Figure 3. Probability density function of simulated annual mean BC e-folding aging time (h) over the globe for a microphysics-based scheme (solid line) and a fixed aging scheme (dashed line). Also shown is 95% uncertainty range (in grey) of the microphysics-based aging time estimated from a Monte Carlo method.



1136
 1137
 1138
 1139
 1140
 1141
 1142
 1143
 1144
 1145

Figure 4. GEOS-Chem simulated annual mean contribution of condensation to total BC aging rate (sum of condensation and coagulation) averaged within 0-1 km above the surface (top left) and zonally (top right) and annual mean contribution of $\text{H}_2\text{SO}_4\text{-HNO}_3\text{-NH}_3$ condensation to the BC aging rate through total condensation (sum of $\text{H}_2\text{SO}_4\text{-HNO}_3\text{-NH}_3$ and SOA condensation) averaged within 0-1 km above the surface (lower left) and zonally (lower right). Model results are for 2009.



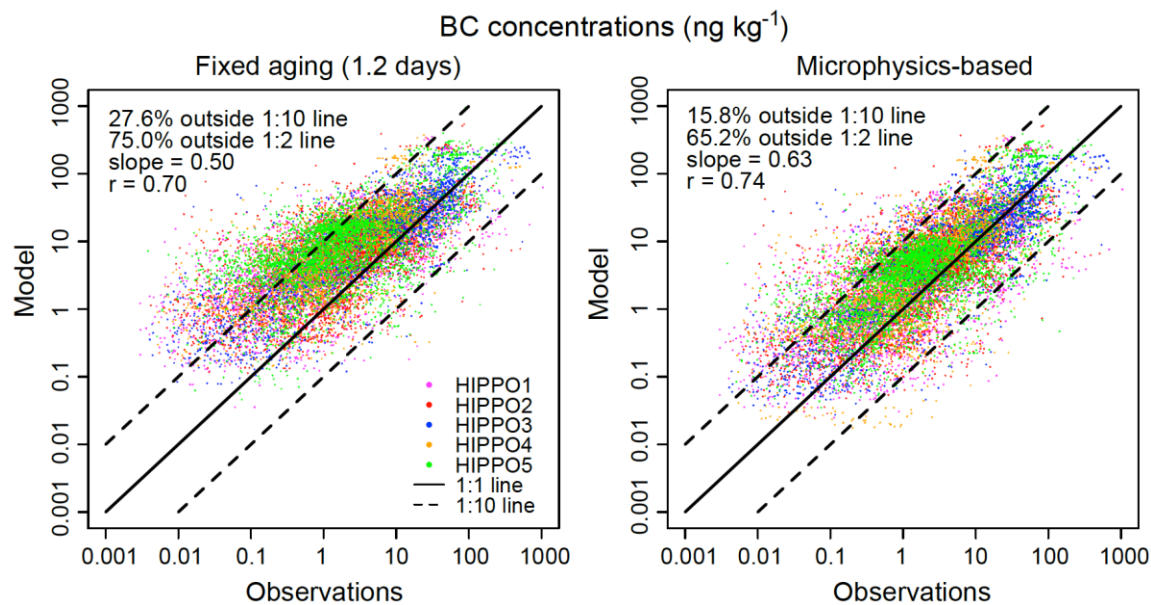
1146

1147

1148 **Figure 5.** Probability density functions of HIPPO observed (black) and GEOS-Chem
 1149 simulated BC concentrations. Model results using a fixed BC aging (blue) and a
 1150 microphysics-based aging (red) are shown. The 95% uncertainty range of the HIPPO
 1151 observations, estimated from a Monte Carlo method, is shown (in grey). Also shown (in
 1152 light red) is the range of model results from microphysics-based sensitivity simulations
 1153 (see Table 1 and text for details). Dashed lines show the median of observations (1.56 ng kg^{-1} ,
 1154 ng kg^{-1} , black), fixed aging (6.55 ng kg^{-1} , blue), and microphysics-based aging (3.52 ng kg^{-1} ,
 1155 red). About 5% of the observed BC concentrations are below 0.01 ng kg^{-1} .

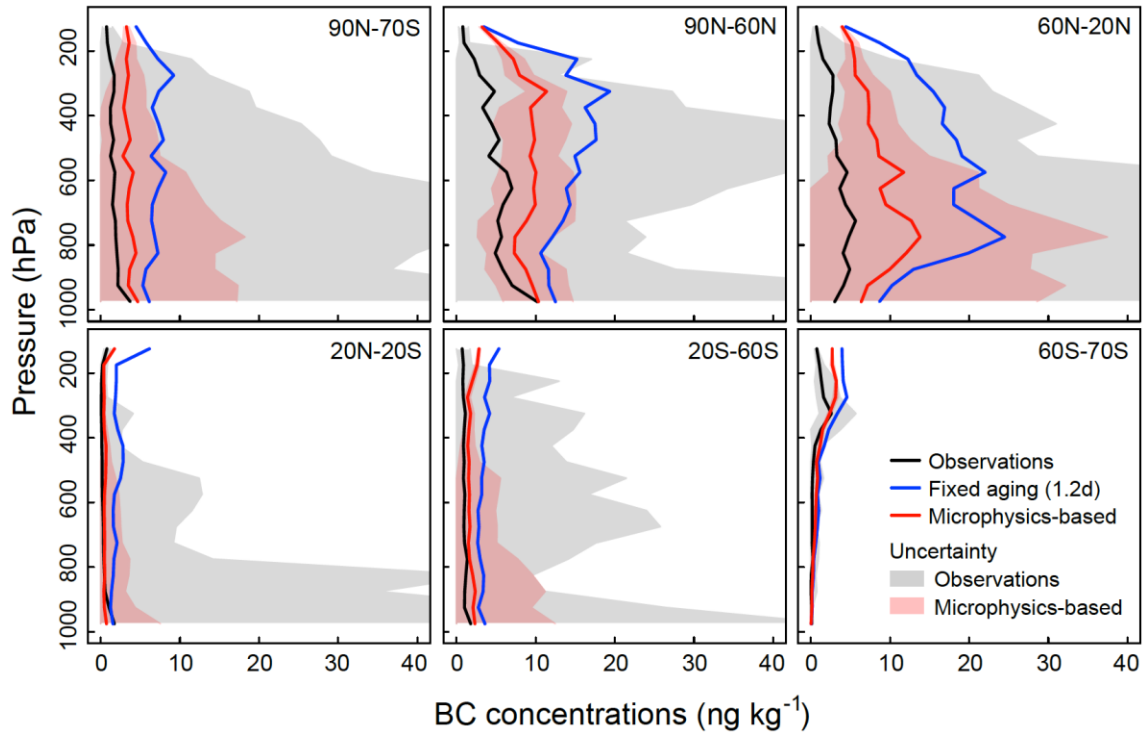
1156

1157



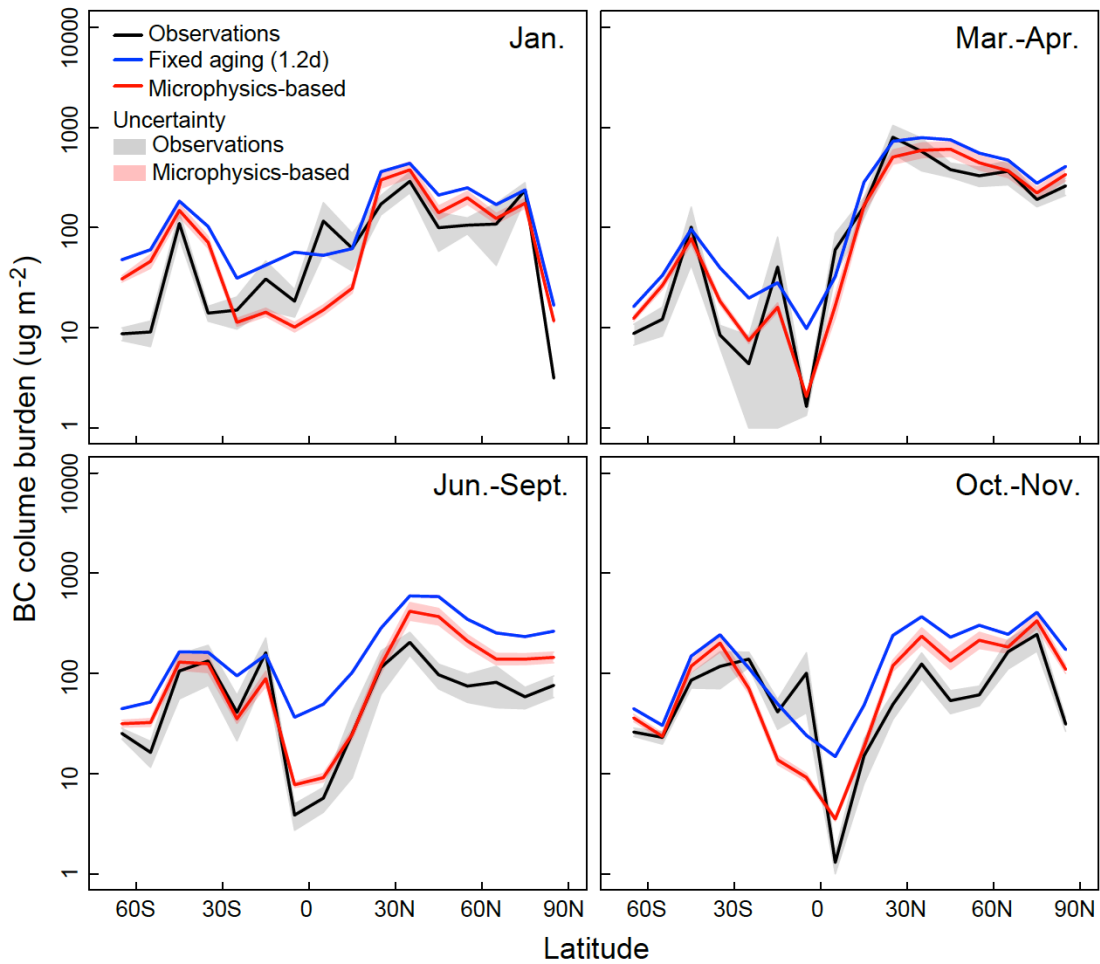
1158
 1159
 1160
 1161
 1162
 1163
 1164
 1165
 1166
 1167
 1168

Figure 6. HIPPO observed and GEOS-Chem simulated BC concentrations sampled along the HIPPO flight tracks (HIPPO 1: pink, HIPPO 2: red, HIPPO 3: blue, HIPPO 4: orange, HIPPO 5: green; see Fig. 1), with model results using a fixed BC aging scheme (left panel) and a microphysics-based BC aging scheme (right panel). Also shown are the 1:1 and 1:10 (or 10:1) ratio lines, percentages of data points outside 1:10 (or 10:1) and 1:2 (or 2:1) ratio lines, and slopes and correlation coefficients (r) of the regression lines between model results and observations.



1169
 1170
 1171
 1172
 1173
 1174
 1175
 1176
 1177
 1178

Figure 7. Median vertical profiles of HIPPO observed (black) and GEOS-Chem simulated BC concentrations at different latitudes. Results are averaged over 50 hPa altitude bins. Model results using a fixed BC aging (blue) and a microphysics-based aging (red) are shown. Also shown are the 1- σ uncertainties of observations (grey) and model results (light red) from microphysics-based sensitivity simulations (see Table 1 and text for details).



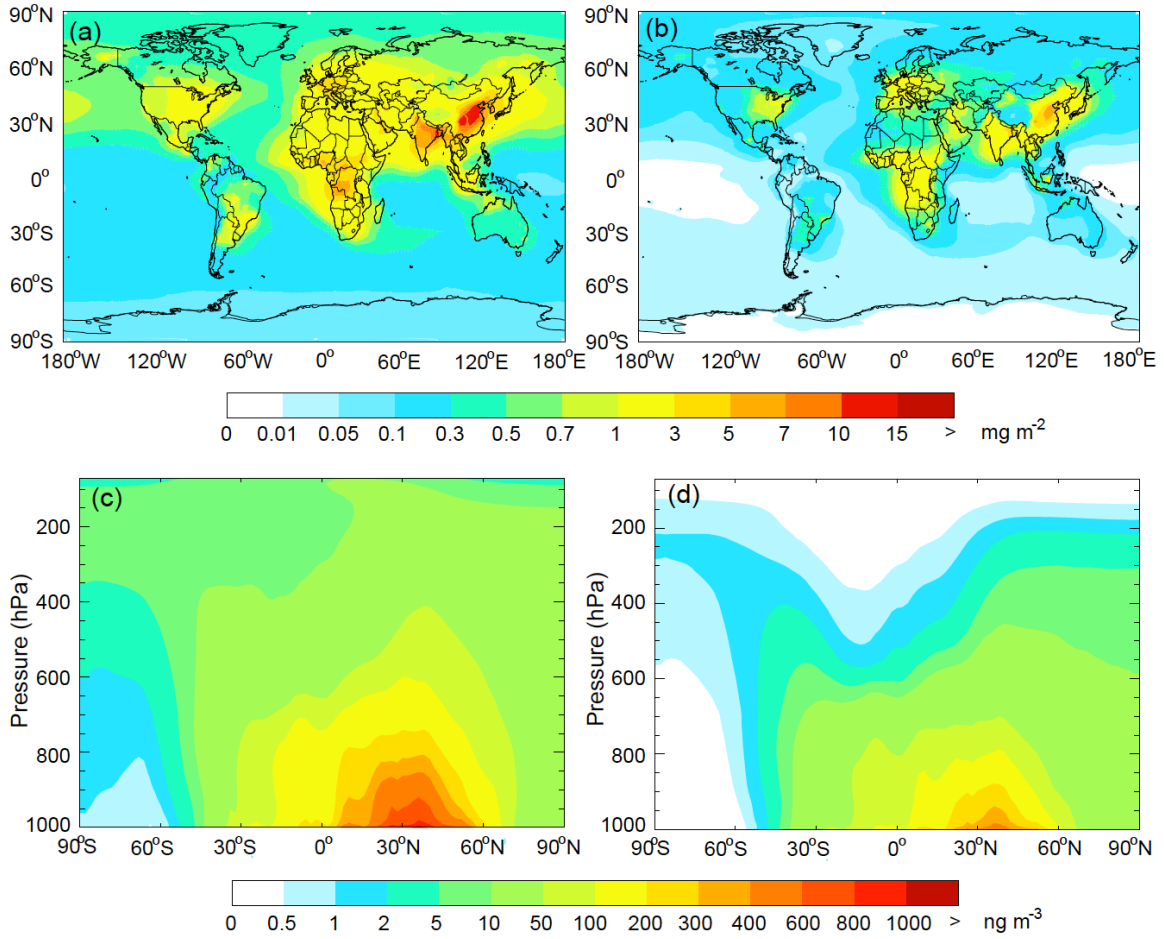
1179

1180

1181 **Figure 8.** Latitudinal distributions of HIPPO observed (black) and GEOS-Chem
 1182 simulated BC column burden ($\mu\text{g m}^{-2}$) in different seasons. The column burden is
 1183 computed by integrating vertical profiles from the surface to 250 hPa (~ 10 km) in 10°
 1184 latitude bins. Model results using a fixed BC aging (blue) and a microphysics-based
 1185 aging (red) are shown. Also shown are the $1-\sigma$ uncertainties of observations (grey)
 1186 and model results (light red) from microphysics-based sensitivity simulations (see Table 1 and
 1187 text for details).

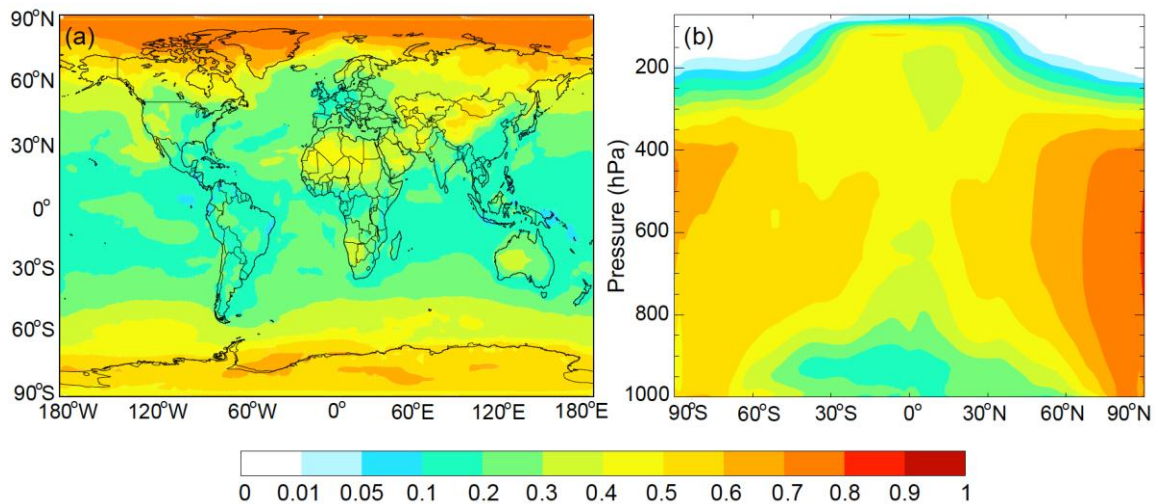
1188

1189



1190
 1191
 1192
 1193
 1194
 1195
 1196
 1197

Figure 9. GEOS-Chem simulated annual mean BC column burden (mg m^{-2}) (top panels) and zonal mean BC concentrations (ng m^{-3}) (lower panels) using a fixed BC aging scheme (left panels) and a microphysics-based aging scheme (right panels). Model results are for 2009.



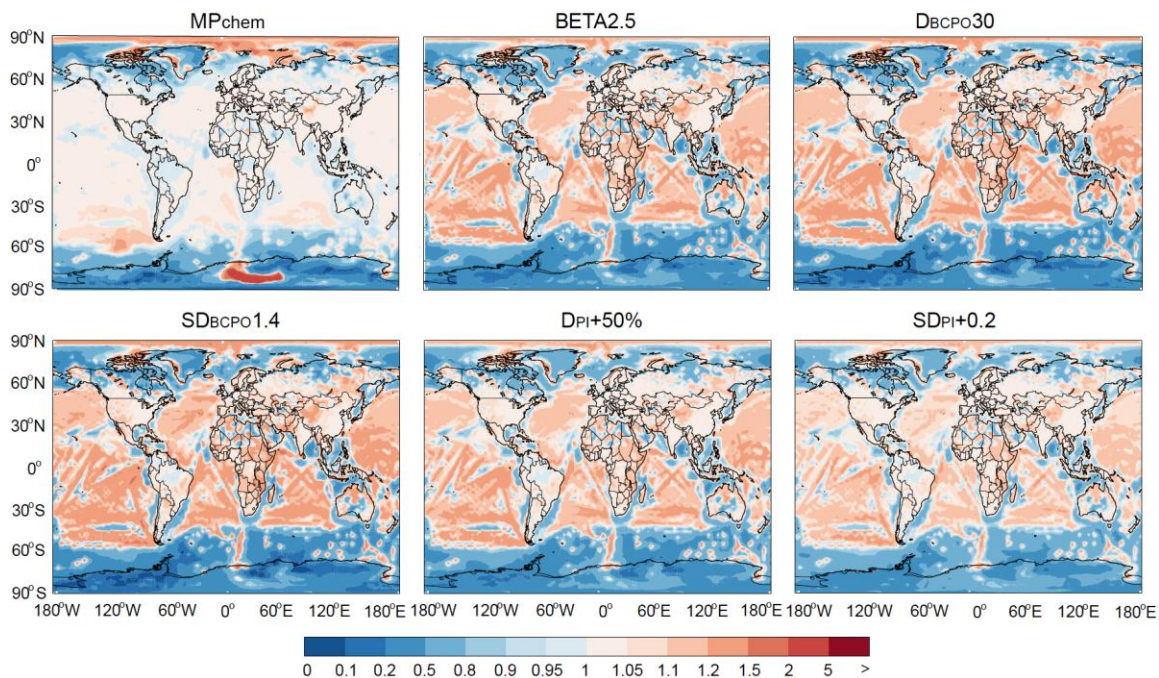
1198

1199

1200 **Figure 10.** GEOS-Chem simulated annual mean contribution of chemical oxidation to the
 1201 total BC aging rate (sum of condensation, coagulation, and chemical oxidation) averaged
 1202 within 0-1 km above the surface (left) and zonally (right). Model results are for 2009.

1203

1204



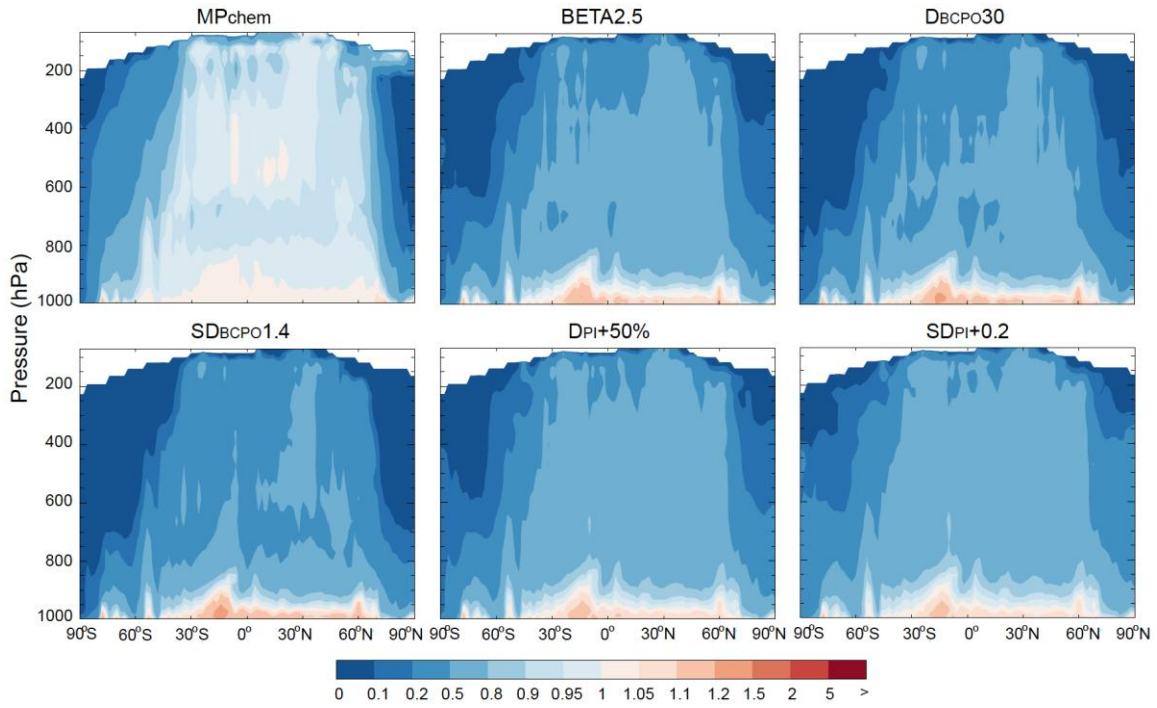
1205

1206

1207 **Figure 11.** GEOS-Chem simulated ratios of annual mean BC aging rate from six
 1208 microphysics-based simulations (Table 1) to that from the standard microphysics-based
 1209 simulation in the surface layer. See Table 1 and text for details. Model results are for
 1210 2009.

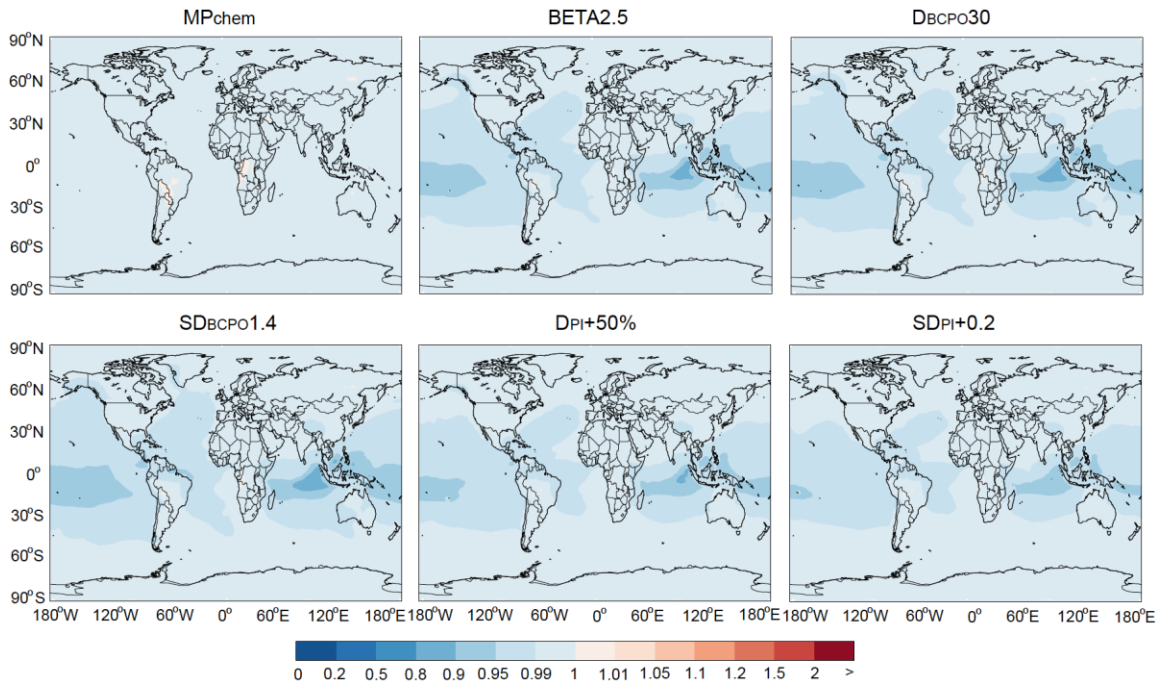
1211

1212



1213
 1214
 1215
 1216
 1217

Figure 12. Same as Fig. 11, but for zonal mean BC aging rate.



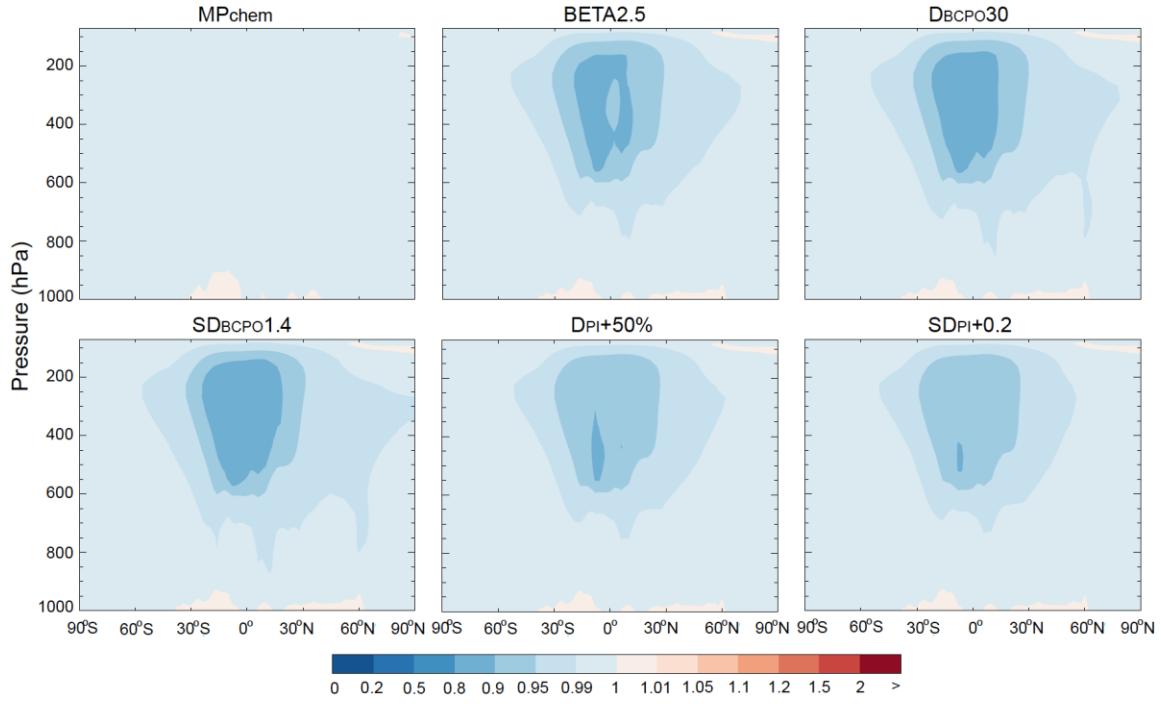
1218

1219

1220 **Figure 13.** Same as Fig. 11, but for BC column burden.

1221

1222



1223
 1224
 1225
 1226

Figure 14. Same as Fig. 12, but for zonal mean BC concentrations.